

Review

Not peer-reviewed version

---

# Nuclear Magnetic Resonance Relaxation Pathways in Electrolytes for Energy Storage

---

[Carla C. Fraenza](#) , [Steve Greenbaum](#) , [Sophia N. Suarez](#) \*

Posted Date: 12 April 2023

doi: 10.20944/preprints202304.0243.v1

Keywords: NMR spin-lattice relaxation time; NMR Fast Field Cycling (FFC); electrolytes



Preprints.org is a free multidiscipline platform providing preprint service that is dedicated to making early versions of research outputs permanently available and citable. Preprints posted at Preprints.org appear in Web of Science, Crossref, Google Scholar, Scilit, Europe PMC.

Copyright: This is an open access article distributed under the Creative Commons Attribution License which permits unrestricted use, distribution, and reproduction in any medium, provided the original work is properly cited.

Review

# Nuclear Magnetic Resonance Relaxation Pathways in Electrolytes for Energy Storage

Carla C. Fraenza <sup>1</sup>, Steve G. Greenbaum <sup>1,2</sup> and Sophia N. Suarez <sup>2,3,\*</sup>

<sup>1</sup> Hunter College of The City University of New York, 695 Park Avenue, New York, NY 10065

<sup>2</sup> Physics Department, The Graduate Center of CUNY, New York, NY 10016

<sup>3</sup> Brooklyn College of The City University of New York, 2900 Bedford Avenue, Brooklyn, NY, 11210

\* Correspondence: snsuarz@brooklyn.cuny.edu

**Abstract:** NMR spin relaxation times have been an instrumental tool in deciphering the local environment of ionic species, the various interactions they engender and the effect of these interactions on their dynamics in conducting media. Of particular importance has been their application in studying the wide range of electrolytes for energy storage, on which this chapter is based. Here we highlight some of the research carried out on electrolytes in recent years using NMR relaxometry techniques. Specifically, studies on liquid electrolytes, such as ionic liquids and organic solvent; on semi-solid-state electrolytes, such as ionogels and polymer gels, and solid electrolytes such as glasses, glass ceramics and polymers. Although this chapter focuses on a small selection of materials, we believe they demonstrate the breadth of application and the invaluable nature of NMR relaxometry.

**Keywords:** NMR spin-lattice relaxation time; NMR Fast Field Cycling (FFC); electrolytes

## 1. Introduction

The need for clean and sustainable energy storage and conversion devices has increased exponentially in the last few decades with the advancement of technology, and concerns about dwindling natural resources and environmental degradations [1-3]. One of the main drivers of this increase has been the worldwide focus on common communications consumer products such as mobile phones, tablets and laptops which are mainly dependent on energy storage devices such as batteries. Another driver of this increase has been renewable energy sources such as wind and solar, which are the fastest growing electricity producers [4-6] with an average increase of 6.3% annually. Although renewable energy sources are weather dependent, the main problem with their increased implementation has been the dissimilarity between their peak production and actual usage-by-consumers times. Because of this, energy storage devices are needed to maximize the efficiency and reliability of renewable energy sources.

Energy storage and conversion devices have differences in their functionalities as well as their ions or species transports. Devices such as batteries and supercapacitors function to produce and store electrical energy through the conversion of chemical energy; while fuel cells and solar cells function to convert chemical and light energy into immediately deliverable electrical energy [2,3,7]. Within each category of devices there are further delineations. For example, the solid oxide fuel cell (SOFC) operates at high temperatures (600 – 1000°C) and relies on the transport of gaseous species through porous ceramics, while the polymer electrolyte fuel cell (PEFC) operates at lower temperatures (< 100°C) and relies on species transport through multiple dissimilar layers and materials.

In terms of storage, the most effective devices are secondary batteries of which the most prevalent have been lithium-ion batteries (LIBs) [4-6,8-11]. Made available by Sony in 1991, they initially powered smaller mobile devices because of their high energy density and longer lifetime compared to other storage devices. However, with the vast number of improvements made since, they have become ubiquitous the world over, powering larger consumer needs such as electric vehicles. In spite of this, serious problems still plague LIBs, mainly safety and cost. Another

electrochemical energy storage device worth mentioning is the supercapacitor. Whereas batteries have the advantage of high energy densities, supercapacitors [1-3,12-17] – although lacking in this regard – have higher power densities and longer life cycles. They also have wide temperature ranges and require lower maintenance compared to LIBs [14], which oftentimes require battery management systems (BMS). They came into commercial application in 1957 when General Electric patented the first electric double layer capacitor (EDLC), in which charge storage is accomplished by the electrostatic separation of charges at the interfaces of the electrodes and electrolyte. Other supercapacitors include the pseudocapacitor – in which charge storage is accomplished through Faradaic processes, and the hybrid capacitor – which is the combination of the EDLC and pseudocapacitor and accomplishes charge storage through both Faradaic and non-Faradaic processes. As mentioned above, supercapacitors suffer from low energy densities, and improving this requires the right combination of electrodes and electrolyte.

## 2. Electrolytes

At the center of these electrochemical storage and conversion devices is an electrolyte, which acts simultaneously as an ion conductor and electron insulator between the electrodes. Its electron-insulating property ensures the charge transfer processes responsible for producing electricity takes place at the electrode-electrolyte interfaces, while its ion conducting property is directly related to the devices' efficiency [18,19]. The electrolyte can also affect the device's cycle stability, electrochemical window of operation, capacity, safety, and other operating conditions [18,19]. In LIB electrolytes, one of the main functionalities of the electrolyte is the formation of the solid electrolyte interphase (SEI) layer [20-28] at the anode. In general, the SEI layer passivates the electrodes and contributes to the Li-ion diffusion processes necessary for energy production. The formation of the SEI layer is a dynamic process that depends on several factors including the type, components and concentrations of the additives and the bulk electrolyte; the specific anode material, its structure and associated surface chemistry. It involves the transformation from initially formed inorganic ( $\text{LiF}$  and  $\text{Li}_2\text{CO}_3$ ) [22,23] and organic (ex. Lithium ethylene decarbonates (LEDC) [20,21] species, which through numerous ageing processes [24-27] such as hydrolysis, reactions between Li salt and intermediate decomposition products, thermal decomposition, and continuous electrolyte reduction [29], its compositional state evolves. Because of the multifaceted dependence of the composition and performance of the SEI layer, the combination of electrodes (especially the anode) and electrolyte must be a merger based upon electrochemical, thermal and mechanical compatibilities.

There are various types of electrolytes including liquids, solids or quasi-solid state, and redox active. Each type of electrolyte is further delineated into subcategories. For example, within the liquid electrolytes are aqueous and non-aqueous types, while the redox electrolytes include gels, ionic liquids, organic, and aqueous types.

Organic liquid electrolytes have been the most applied in secondary battery applications [20,21,24-27,30-37]. The basic component of organic electrolytes are organic solvents and some of their properties should include high dielectric constants ( $> 15$ ) which facilitates salt dissociation and reduces ion pairing. The organic solvent should also have low viscosity which enhances high ionic mobility. Additionally, the solvent should be electrochemically stable in its interactions with the electrodes. In the case of LIBs, liquid electrolytes are usually a combination of a lithium salt such as lithium hexafluorophosphate ( $\text{LiPF}_6$ ), lithium tetrafluoroborate ( $\text{LiBF}_4$ ), lithium perchlorate ( $\text{LiClO}_4$ ), or lithium trifluoromethanesulfonate ( $\text{LiCF}_3\text{SO}_3$ ), dispersed in one or more non-aqueous solvents such as dimethyl carbonate (DMC), diethyl carbonate (DEC), propylene carbonate (PC), or ethylene carbonate (EC). These organic carbonates are generally flammable and volatile, and when combined with alkali salts such as  $\text{LiPF}_6$  which have limited thermal stability and are sensitive towards hydrolysis, the result can be unsafe for consumers through heat generation, thermal runaway, cell venting, fire and even explosion. The inclusion of film-forming additives such as fluoroethylene carbonate (FEC), and vinylene carbonate (VC); and flame-retardant additives such as trimethyl

phosphate (TMP) and triethyl phosphate (TEP), offer improvements in the electrolytes by providing more stable SEI layers and lowered flammability or the organic solvents [38-40].

Ionic liquids (ILs) have also gained increasing attention as electrolytes and electrolyte solvents in the last decade [41-48]. ILs possess low volatility, low to zero flammability, wide electrochemical ranges (up to 6V), and fairly good ionic conductivities. The use of pure ILs as electrolytes have been hindered by their relatively high solution viscosities. The incorporation of organic additives to ILs have been shown to improve the mixtures' ionic conductivities, and the use of additives can offer more effective SEI layers [42]. The most used ILs consist of imidazolium-based cations [41-48] such as imidazolium, pyridinium, piperidinium and pyrrolidinium, all of which are classified as aprotic. The most commonly used anions include bis(trifluoromethylsulfonyl)amide ( $(\text{CF}_3\text{SO}_2)_2\text{N}^-$ ), hexafluorophosphate ( $\text{PF}_6^-$ ) and tetrafluoroborate ( $\text{BF}_4^-$ ). On the other hand, deep eutectic solvents (DESs) [36,37,49-54], which sometimes are considered a sub-class of ILs due to their similar properties, have shown to be promising as electrolytes as well [36,37,49-54]. These solvents are defined as a mixture of two or more components, which may be solid or liquid and that at a particular composition present a high melting point depression becoming liquids at room temperature. Unlike typical ILs, DESs can be inexpensive, readily synthesized, and can often be prepared from biodegradable, and nontoxic constituents.

Semi-solid-state electrolytes (SSEs) have attracted interest because they combine the main advantages of liquid and solid electrolytes, namely the high ionic conductivity and mechanical stability respectively. Among them are solid polymer electrolytes (SPEs), ionogels (IGs) and gel polymer electrolytes (GPEs). IGs consist of an IL electrolyte confined in a mesoporous inorganic matrix which macroscopically behaves as a solid, but at the nanoscale a liquid-like state is maintained [55-60], while GPEs consist of a gelled polymer matrix swollen in a liquid electrolyte [61,62]. Due to their optimal interfacing with electrodes and liquid-like transport behavior, GPEs have found application in commercial LIBs [63,64]. Although less investigated compared to liquid electrolytes, SPEs offer several advantages over liquids due to their flexibility, adhesion to electrodes, volumetric compactness, general accommodation of volumetric changes in the electrodes, and safety [65-68]. This is why solid-state batteries are generally not affected by ionic short circuits and can therefore be assembled into higher voltage battery stacks without external separation between each cell [69]. The most studied type of SPEs is based on poly (ethylene oxide) (PEO), into which a salt has been dissolved [70-74]. However, its electrolytes generally suffer from very low ionic conductivities ( $\leq 10^{-6}$  S/cm) and low transport numbers ( $t_{\text{Li}^+} \sim 0.2 - 0.3$ ) [75,76] due to the strong coordination of lithium ions with the oxygen atoms in the PEO backbone [77-79]. In spite of this, studies on PEO persists [80-83] with researchers focused on modifications that will enhance  $\text{Li}^+$  transport.

### 3. NMR Relaxation

Measurements of NMR spin relaxation times have become an important investigative tool in the study of dynamics in materials. The relaxation times most commonly determined are spin-lattice ( $T_1$ ), spin-spin ( $T_2$ ), and the Nuclear Overhauser Effect (NOE) [84-90]. Regardless of the type, spin relaxation is caused by temporal fluctuating interactions and the associated relaxation time depends on the strength and type of interactions, as well as the spectral density functions ( $J(\omega)$ ). These temporal fluctuations are from the local magnetic field, or in the case of quadrupole nuclei – the local electric field gradient (EFG) – at the site of the affected spin. Fundamentally, the spectral density functions provide information on the power available for causing spin transitions among the different frequencies [88]. More expressly, it is the Fourier Transform of the time dependent correlation function  $G(\tau)$ , which is associated with a correlation decay time constant ( $\tau_c$ ) for the associated dynamical process (see Eq. (1)).

$$J(\omega) = A \int_{-\infty}^{\infty} G(\tau) e^{-i\omega\tau} d\tau.$$

(1)

Here  $A$  represents a normalization coefficient, and  $\omega$  represents the angular frequency in rads/s. Simplistically,  $\tau_c$  is defined as the time in which a molecule remains in any given position before a collision causes it to change position or orientation. Generally, rapid fluctuations result in small  $\tau_c$ , while slow fluctuations have larger  $\tau_c$ . Since the focus of this paper is on the applications of relaxation times, we will provide a brief review of those applications most commonly studied. However, for a more in-depth treatise on spin relaxation times and the associated mechanisms the interested reader is directed to the various references cited [84-90].

Spin-lattice or longitudinal relaxation is the process by which the radiofrequency excited net spins or the magnetization component along the quantization field ( $M_z$ ) returns to thermal equilibrium. Because  $M_z$  is determined by the quantized nuclear spins,  $T_1$  relaxation is determined only by transitions that change the nuclear spin state and energy [85]. The recovery of  $M_z$  to equilibrium is governed by the equation:

$$M_z = |M_0| \left(1 - e^{-t/T_1}\right),$$

(2)

where  $M_0$  and  $t$  represent the equilibrium magnetization as per the Curie law, and the time elapsed after the completion of the radiofrequency excitation field. If the fluctuations in the local magnetic field or the EFG are due to thermally activated motions, then the temperature or magnetic field (ergo resonance frequency  $\omega_0$  in rad/s) dependent  $T_1$  can provide information on the motional process. Associated with this process is a rate constant  $R_1 = 1/T_1$ , that provides details on motions with rates similar to the Larmor frequency, and when measured as a function of temperature allows determination of the activation energies of dynamical processes. Moreover, when  $R_1$  is measured as a function of frequency, it provides straightforward access to the frequency-dependent spectral density  $J(\omega)$  according to [91]:

$$R_1(\omega) = K[J(\omega) + 4J(2\omega)], \quad (3)$$

where  $K$  is a constant that describes the strength of the dominating spin interaction, which can be dipolar ( $K=A_{DD}$ ) or quadrupolar ( $K=A_Q$ ).

Spin-spin (also termed transverse) relaxation is the process of transverse decoherence. A simple visualization of this process is the decay of the magnetization in the transverse plane of a perfectly homogeneous quantization field following a  $(\pi/2)_x$  radiofrequency excitation pulse. Since the transverse components of the equilibrium magnetization ( $M_x$  and  $M_y$ ) are the result of spins precessing with nonrandom phases, transverse relaxation can be affected by any interaction that results in phase changes including isoenergetic ones [85]. The decoherence is governed by the equation:

$$M_{x,y} = |M_0| e^{-t/T_2}.$$

(4)

Associated with this process is a rate constant  $R_2 = 1/T_2$  which – in the case of a perfectly homogeneous quantization field and Lorentzian spectrum – is related to the line width at half maximum [94] through the relationship  $R_2 = \pi\nu_{1/2}$ .  $R_1$  provides details on motions at zero frequency.

The Nuclear Overhauser Effect (NOE) refers to the net change in the signal intensity of the enhanced spin  $I$  due to the relaxation of the perturbed spin  $S$  in a dipole-dipole (DD) coupled spin system [86]. Since the NOE depends on the DD interaction, modulating fluctuations due to molecular motion can produce cross relaxation and magnetization transfer. Like the DD interaction, the NOE depends on the inverse sixth power of the internuclear distance ( $r_{IS}^{-6}$ ) between spins  $I$  and  $S$ . Because of this, neighboring spins must be within 5 Å for NOE applications. Associated with the NOE are the cross-relaxation rate ( $\sigma_{IS}$ ) and dipolar longitudinal relaxation ( $\rho_{IS}$ ) rates, given by:

$$\sigma_{IS} = \left(\frac{\mu_0}{4\pi}\right)^2 \frac{\hbar^2 \gamma_I^2 \gamma_S^2}{10} \left( \frac{6\tau_c}{1+(\omega_I + \omega_S)^2 \tau_c^2} - \frac{\tau_c}{1+(\omega_I - \omega_S)^2 \tau_c^2} \right) r_{IS}^{-6}, \quad (5)$$

$$\rho_{IS} = \left(\frac{\mu_0}{4\pi}\right)^2 \frac{\hbar^2 \gamma_I^2 \gamma_S^2}{10} \left( \frac{6\tau_c}{1+(\omega_I + \omega_S)^2 \tau_c^2} + \frac{3\tau_c}{1+\omega_I^2 \tau_c^2} + \frac{\tau_c}{1+(\omega_I - \omega_S)^2 \tau_c^2} \right) r_{IS}^{-6}. \quad (6)$$

Here  $\gamma_I$  and  $\gamma_S$  are the magnetogyric ratios of spins I and S respectively, and  $\mu_0$  is the magnetic permeability of vacuum. Although initially intended for intramolecular spins, the NOE has recently been applied to intermolecular spins interactions in highly viscous ILs media [92-95]. This is in spite of additional modulations of the intermolecular DD interaction by the translational motions of the molecules. Examples of these will be discussed.

#### 4. Translational and Rotational Dynamics in Liquid and Confined Electrolytes

In studies of the dynamics in liquid ILs and LIB electrolytes, measurements of  $T_1$  have been the most ubiquitous. As previously stated, associated with the dynamic processes is a correlation function  $G(\tau)$  (or distribution) and  $\tau_c$  [84-90]. In order to properly analyze the dynamics researchers often need to assume a priori what the responsible relaxation mechanism or mechanisms are. In general, there are five main mechanisms for spin relaxation:

$$\frac{1}{T_1} = \frac{1}{T_1^{DD}} + \frac{1}{T_1^{CSA}} + \frac{1}{T_1^{SR}} + \frac{1}{T_1^{SC}} + \frac{1}{T_1^Q},$$

(7)

where  $T_1^{DD}$ ,  $T_1^{CSA}$ ,  $T_1^{SR}$ ,  $T_1^{SC}$ , and  $T_1^Q$  represent the DD, chemical shift anisotropy (CSA), spin rotation (SR), scalar coupling (SC), and quadrupolar interactions (Q) relaxation times respectively. In the case of liquids with spin  $I = 1/2$  nuclei such as  $^1\text{H}$  and  $^{19}\text{F}$ , oftentimes intramolecular and intermolecular DD interactions are the dominant relaxation mechanisms. Both DD interactions are modulated in time by molecular rotations and the relative translational diffusion of molecules carrying the nuclear spins [89]. Because of this, the  $T_1$  profiles of ILs can be modeled by considering these two molecular motions. Spin rotation and scalar couplings become significant when small molecules are involved. In the case of quadrupolar nuclei such as  $^2\text{H}$ ,  $^7\text{Li}$ ,  $^{11}\text{B}$  and  $^{23}\text{Na}$ , the quadrupole interaction usually dominates.

The main model used in relaxation times analyses is the Bloembergen, Purcell, and Pound (BPP) [84-91]. In this model the correlation function  $G(\tau)$  is given the simple form of a time dependent decaying exponential of the form  $\sim \exp(-t/\tau_c)$ . When a plot of  $T_1$  versus inverse temperature is done, the BPP model predicts a symmetric v-shaped curve. However, when applied to highly viscous, quadrupolar nuclei or solid media, deviations arise due to the local distribution of interactions ergo the heterogeneous nature of the material. In these cases, the correlation function is better represented as a stretched exponential of the form  $\sim \exp(-t/\tau_c)^\beta$ , where  $\beta$  represents the distribution of interactions strengths throughout the media and ranges between 0 and 1.

##### 4.1. Ionic Liquids Dynamics

One of the main probes of ion dynamics in ILs has been through the use of dilute solute particles such as benzene, carbon monoxide (CO) and carbon dioxide ( $\text{CO}_2$ ). The rationale for this is that the solute (ergo probe) dynamics will be dependent upon its interactions with the cations and anions and that by using probes one can get a microscopic view of the ILs' local structure. The following studies highlight this rationale.

Yasaka et.al. [96] used  $^{17}\text{O}$   $T_1$  to probe the rotational dynamics of CO in 1-ethyl-3-methylimidazolium bis(trifluoromethanesulfonyl)imide ( $[\text{C}_2\text{C}_{1\text{im}}][\text{NTf}_2]$ ), 1-butyl-3-methylimidazolium ( $[\text{C}_4\text{C}_{1\text{im}}]$  NTf<sub>2</sub>, and 1-methyl-3-octylimidazolium ( $[\text{C}_8\text{C}_{1\text{im}}]$  NTf<sub>2</sub>. In the 'extreme narrowing' limit ( $\omega_0\tau_c \ll 1$ ) of the BPP model, the  $T_1$  for a quadrupolar nucleus exposed to an axially symmetric electric field gradient is given by:

$$\frac{1}{T_1} = \frac{3\pi^2}{10} \frac{(2I+3)}{I^2(2I-1)} \left(\frac{e^2Qq}{h}\right)^2 \tau_R,$$

(8)

where  $e^2Qq/h$  is the quadrupolar coupling constant (QCC). For all three ILs,  $\tau_R$  was  $\leq 10$  ps and between 295 – 413K decreased by one order of magnitude due to the reduction in viscosity. The authors used the Stokes-Einstein-Debye (SED) equation:

$$\tau_R = \frac{\eta fVC}{k_B T}$$

(9)

to determine if there were deviations between the respective correlation times. Here  $V$  is the Van der Waals volume of the solute,  $C$  is the boundary condition parameter with values between  $C_{\text{slip}}$  (0) and  $C_{\text{stick}}$  (1),  $f$  is the shape parameter that accounts for the non-spherical nature of solutes,  $k_B$  is Boltzmann constant,  $T$  is the absolute temperature, and  $\eta$  is the solution viscosity. The results of the CO dynamics evaluated by the SED equation were 10 to 100 times faster than the predicted slip hydrodynamic values and were classified in the superslip regime. The importance of this result is that it separates the impediments to the rotational motion of the CO molecule from the ILs' viscosity effects. The authors also investigated the effect of increasing alkyl chain length on the CO molecule's rotational dynamics and determined that at fixed  $\eta/T$  values  $\tau_R$  decreased. In other words, as the size of the nonpolar domain increases so does the CO molecule's rotation. They also found a fractional SED relationship ( $\tau_R \propto (\eta/T)^p$ ) between  $\tau_R$  and  $\eta/T$  which the authors surmised was due to the Van der Waals volume difference between the solute and solvent molecules. Here the constant  $p$  represents the degree of deviation of  $\tau_R$  from the SED relationship.

In a similar more expansive and recent study, Endo et.al. [97] also used  $^{17}\text{O}$   $T_1$  in their study of 10 NTf<sub>2</sub><sup>-</sup> anion based ILs. The cations included four imidazolium- ( $\text{C}_1\text{C}_0\text{im}^+$ ,  $\text{C}_1\text{C}_2\text{im}^+$ ,  $\text{C}_1\text{C}_4\text{im}^+$ ,  $\text{C}_1\text{C}_6\text{im}^+$ ), four phosphonium- ( $\text{P}_{2225}^+$ ,  $\text{P}_{4448}^+$ ,  $\text{P}_{44412}^+$ ,  $\text{P}_{8884}^+$ ), and two ammonium- ( $\text{N}_{4441}^+$ ,  $\text{N}_{8884}^+$ ) based types. The  $T_1$  data all fell into the motional narrowing regime and like the Yasaka study [96], the  $\tau_R$  values were faster than the SED predictions with the slip boundary condition. Fits of  $\tau_R$  vs.  $\eta/T$  were also non-linear which the authors surmised was due to free rotation-like motion of the CO molecules. The authors also found increasing deviation of  $\tau_R$  from SED predictions with an increase in the number of carbon atoms in the alkyl chain, in spite of the cation type. CO molecules are expected to reside closer to the alkyl chains and results show their rotation occur within 1 ps, making them generally insensitive to the viscosity effects. This result supports the dissimilarities between local environments of the cations' head groups and their alkyl chains.

In a related study Rumble et.al. [38] used  $^2\text{H}$   $T_1$  to study the dynamics of dilute deuterated benzene ( $\text{C}_6\text{D}_6$ ) in [ $\text{C}_4\text{C}_1\text{im}$ ] tetrafluoroborate ( $[\text{BF}_4]$ ), and two deuterated versions of the  $\text{C}_2\text{C}_1\text{im}^+$  cation ( $\text{C}_2\text{C}_1\text{im}^+\text{-d}_1$  and  $\text{C}_2\text{C}_1\text{im}^+\text{-d}_6$ ) in  $\text{C}_2\text{C}_1\text{im}^+$  NTf<sub>2</sub>. The uniqueness of this study lies with the authors' use of three different magnetic field strengths in which the  $^1\text{H}$  Larmor frequencies were 300, 400 and 850 MHz for the determination of the  $^2\text{H}$   $T_1$  measurements. The purpose of this was to explore the applicability of the 'extreme narrowing' condition that is often used in analyzing ILs' dynamics. Over the temperature range investigated (240 – 320 K) the authors found agreement between the extreme narrowing regimes at the three frequencies for all three probe molecules. Like the Yasaka et.al. study [96], their calculated  $\tau_R$  values for the  $\text{C}_6\text{D}_6$  probe molecule expressed as a function of  $\eta/T$  also showed deviations from the hydrodynamic predictions and were instead related by the fractional SED. Through the combination of Molecular Dynamics Simulations (MDS) and the relaxation studies the authors' showed there were differences between the dynamics of the  $\text{C}_6\text{D}_6$  probe molecule in conventional organic solvents and ILs. When spun about its 6-fold axis the dynamics was similar in both media and faster than predicted by the hydrodynamic predictions. However, 'tumbling' rotation about in-plane axes was more impeded in ILs due to their higher viscosities, resulting in even greater deviations from the hydrodynamic predictions.

On the other hand, Strate et.al. [98] studied the relationship between the rotational and translational dynamics of ions and the hydrogen bond lifetimes, in order to provide information on the structural properties of ILs. They focused on the IL (2-hydroxyethyl) trimethylammonium bis-(trifluoromethylsulfonyl)imide ([Ch][NTf<sub>2</sub>]) and measured deuteron quadrupolar relaxation rates (<sup>2</sup>H R<sub>1</sub>) at 500MHz (<sup>1</sup>H Larmor frequency) of the OD hydroxyl groups of the cation in the deuterated IL as a function of temperature as a way to calculate the reorientational correlation time τ<sub>OD</sub> of this group. They used the equation (7) to obtain τ<sub>OD</sub>, where the QCC was calculated by using its relationship with proton chemical shifts <sup>1</sup>H δ, and within the temperature range between 303 K and 406 K, the τ<sub>OD</sub> values decrease from 32.4 ps to 3.1 ps. This hydroxyl group is involved in the doubly ionic hydrogen bond with the oxygen of [NTf<sub>2</sub>]; therefore, the authors concluded that both modes, rotation and translation of the cation, were affected by the formation and lifetime of doubly ionic hydrogen bonds in the IL. Based on the good agreement between the measured and simulated reorientational correlation times as a function of temperature, they computed self-diffusion coefficients and hydrogen bond lifetimes by means of molecular dynamics simulation. Surprisingly, the magnitude of the self-diffusion coefficient of both cations and anions was found to be similar over the whole temperature range, suggesting that both species diffuse as hydrogen-bonded ion pairs. Additionally, the calculated hydrogen bond lifetime consisted of two separate time domains, namely, short- and long-time contributions. The short-time behavior was within the picosecond time range, showing time constants very similar to the computed reorientational correlation times. However, long-time part was in the nanosecond range and was attributed to exchange based on translational diffusion. Since the long-time contribution of the hydrogen bond lifetime amounts to about two thirds of the overall lifetime, the authors concluded that long-living hydrogen-bonded ion pairs do exist in this particular ionic liquid.

The Fast field cycling (FFC) relaxometry technique [99,100] has been widely used to study molecular motions of ions in ILs [45,60,101-111] due to its outstanding ability to reveal information about translational and rotational dynamics in only one experiment. Although FFC-NMR is a low-resolution technique, it is possible to study dynamics of cations and anions independently if they are composed of different NMR active nuclei. For instance, if the IL composed of 1-butyl-3-methylimidazolium bis(trifluoromethylsulfonyl)imide ([BMIM] TFSI) is considered, according to the chemical structure of the cation and anion, studying the relaxation rate of <sup>1</sup>H and <sup>19</sup>F is equivalent to studying molecular dynamics of BMIM<sup>+</sup> and TFSI<sup>-</sup>, respectively [60,102].

As previously stated, the T<sub>1</sub> dispersions of ILs can be modeled by considering translational and rotational motions that modulate in time the intermolecular and intramolecular interactions. In general, intramolecular dipolar interactions fluctuate in time more rapidly compared to the intermolecular ones and would therefore be effective for relaxation at short time scales. This means its effect would show up in the high field (high Larmor frequency) regime of the spin-lattice relaxation profile. On the other hand, intermolecular interactions are mostly dependent on the translational motion of the whole molecule, which is slower, and therefore efficient for relaxation in the low field regime (low Larmor frequency). Then, in the limit of low Larmor frequencies, the relaxation rate can be expressed as R<sub>1</sub>(ν) ≅ B - A√ν, where A and B are constants. B represents the relaxation contribution from rotational dynamics and A is given by [112-114]:

$$A = \left(\frac{\mu_0}{4\pi}\right)^2 n \gamma^4 \hbar^2 \left(\frac{8\sqrt{2}+2}{15}\right) \left(\frac{\pi}{D_{12}}\right)^{3/2}.$$

(10)

Here μ<sub>0</sub> is the permeability of free space, γ is the gyromagnetic ratio, n is the nuclear density and D<sub>12</sub> is the relative diffusion coefficient defined as the sum of the self-diffusion coefficients of the involved molecular-pair (D<sub>12</sub> = D<sub>1</sub> + D<sub>2</sub>). In the case of identical molecules, D<sub>12</sub> is equal to two times the self-diffusion coefficient. Then, by plotting the spin-lattice relaxation rate values as a function of the square root of the Larmor frequency ν, R<sub>1</sub>(ν) vs. ν<sup>1/2</sup> shapes into a linear function at lower frequencies and D<sub>12</sub> can be easily calculated from the parameter A. The importance of this approximation is the fact that it does not depend on the model used to describe the complete relaxation profile and it



allows to calculate the diffusion coefficient of the ions in ILs, whose values has been shown to be in agreement with the ones obtained with the standard pulsed field gradient (PFG-NMR) diffusion technique [45,101,109].

In spite of the fact that in general ILs consist of interacting non-spherical ions, the force-free-hard-sphere (FFHS) model [112,113] has been employed successfully to describe the spin-lattice relaxation due to translational diffusion in these systems [45,60,101-111,115,116]. Considering that there are no previous studies that extend this diffusion model for elongated molecules, it may be considered as a very first approximation to describe the translational diffusion in ionic liquids. This model is based on the assumption that the molecular motion can be compared to that of a rigid sphere that obeys Fick's diffusion equation, the spins are positioned in the center of the molecules, and there is a uniform distribution of the molecules outside the distance of the closest approach  $d$ . This last one imposes a boundary value condition due to the fact that spin-pair interactions are neglected for interspin distances that are shorter than the distance  $d$ . This excluded volume effect is treated by including an extra term in the relative diffusion equation, representing the potential from averaged forces between the spin-bearing molecules [112,113]. This model provides an approximate but improved description of the system, as compared with the approach used by other authors [117], where the excluded volume effect was not considered. The general expression of  $R_1$  for three-dimensional translational diffusion given by the FFHS model is as follows [112]:

$$R_{1\text{Diff}} = \frac{108}{5} \left( \frac{\mu_0}{4\pi} \gamma^2 \hbar \right) \frac{1}{d^3} n \int_0^\infty \frac{u^4}{81+9u^2-2u^4+u^6} \left[ \frac{\tau_{\text{Diff}}}{u^4+(\omega\tau_{\text{Diff}})^2} + \frac{4\tau_{\text{Diff}}}{u^4+(2\omega\tau_{\text{Diff}})^2} \right] du. \quad (11)$$

Here the correlation time  $\tau_{\text{Diff}}$  is defined as  $\tau_{\text{Diff}} = \frac{d^2}{D_{12}}$ , where  $D_{12}$  is the relative diffusion coefficient and  $u$  is a dimensionless integration variable. This model can take a quite simple expression by assuming that the diffusion can be represented by finite jumps, in the Brownian limit  $r^2/6d^2 \rightarrow 0$ , where  $r^2$  is the mean square jump distance defined by  $r^2 \equiv 6D\tau$ ,  $\tau$  is the mean time between jumps and  $D$  is the self-diffusion coefficient. Then, it is possible to arrive at the following expression for the homonuclear translational relaxation rate  $R_1$  [84,118]:

$$R_{1\text{Diff}}^{ii}(\omega_i) = \frac{A_D^{ii}}{d_{ij}D_{ii}} \left[ \tilde{J}(z(\omega_i)) + 4\tilde{J}(z(2\omega_i)) \right], \quad (12)$$

where  $\omega = 2\pi\nu$  and  $\nu$  is the Larmor frequency;  $A_D = \frac{8}{45} \pi \gamma^4 \hbar^2 \left( \frac{\mu_0}{4\pi} \right)^2 n$ ;  $z(\omega) \equiv \sqrt{2\omega d^2/D_{12}}$ ,

$$\text{and } \tilde{J}(z) = \frac{1 + \frac{5}{8}z + \frac{z^2}{8}}{1 + z + \frac{z^2}{2} + \frac{z^3}{6} + \frac{z^5}{81} + \frac{z^6}{648}}.$$

For heteronuclear translational relaxation,  $R_1$  takes the following expression [84,118]:

$$R_{1\text{Diff}}^{ij}(\omega_i) = \frac{A_D^{ij}}{d_{ij}D_{ij}} \left[ \tilde{J}(z(\omega_i - \omega_j)) + 3\tilde{J}(z(\omega_i)) + 6\tilde{J}(z(\omega_i + \omega_j)) \right]. \quad (13)$$

Here  $A_D^{ij} = \frac{1}{9} \gamma_i^2 \gamma_j^2 \hbar^2 \left( \frac{\mu_0}{4\pi} \right)^2 n_j$ , and the subscripts  $i$  and  $j$  refer to the two different nuclei. Equations (12) and (13) have been used successfully to describe translational relaxation of  $^1\text{H}$  and  $^{19}\text{F}$  in the IL electrolyte composed of [BMIM][TFSI] with up to 1M LiTFSI at different temperatures in the range 303-333K [60]; and in the case of [P<sub>4441</sub>][TFSI] (tributyl methyl phosphonium bis(trifluoromethanesulfonyl)imide) and [N<sub>4441</sub>][TFSI] (tributyl methyl ammonium bis(trifluoromethanesulfonyl)imide) with up to 0.6 molal concentration of LiTFSI at different temperatures in the range 298-338 K [108].

On the other hand, if isotropic molecular rotations with an average correlation time are assumed as a first approach, a Lorentzian function (L) can express the contribution of molecular rotations to the spin-lattice relaxation rate [84-91]:

$$R_{1\text{rot}}^L(\omega) = A_R \left[ \frac{\tau_R}{1+(\omega)^2\tau_R^2} + \frac{4\tau_R}{1+(2\omega)^2\tau_R^2} \right], \quad (14)$$

where  $A_R = \frac{3}{10} \gamma^4 \hbar^2 \left( \frac{\mu_0}{4\pi} \right)^2 \frac{1}{r^6}$  is the corresponding amplitude reflecting the strength of the relevant dipolar interactions,  $r$  is the effective distance between two nuclei located in the same molecule and

$\tau_R$  is the average rotational correlation time. Even though this is the simplest model for rotational relaxation, it has been applied with great success to describe intramolecular relaxation in ILs and IL electrolytes [60,102,103,106,108,115,116]. Other works have considered more realistic models where the high viscosity of ILs, a distribution of motional correlation times and the molecular anisotropy of ions have been taken into account [101,104,119]. However, the mathematical expressions of these models are more complex, and more parameters need to be calculated. Specifically, a Cole-Davidson (CD) form [101,104,109] has been used to describe rotational dynamics:

$$R_{1rot}^{CD}(\omega) = A_R \left[ \frac{\sin(\beta \arctan(\omega\tau_{CD}))}{\omega(1+(\omega\tau_{CD})^2)^{\beta/2}} + \frac{2\sin(\beta \arctan(2\omega\tau_{CD}))}{\omega(1+(2\omega\tau_{CD})^2)^{\beta/2}} \right]. \quad (15)$$

Here the rotational correlation time is given by  $\tau_R = \beta\tau_{CD}$ , where  $0 < \beta \leq 1$  is a phenomenological stretching parameter and for  $\beta = 1$  a Lorentzian form is obtained, and  $\tau_{CD}$  is the average correlation time. In this model, the rotational motion is described as thermally activated jumps over potential barriers where  $\beta$  describes the spread of them, or in other words this parameter is connected to the existence of a distribution of correlation times.

For elongated ions which experience anisotropic reorientations, Woessner's model (W) considers different correlation times for reorientations around the short ( $\tau_S$ ) and long ( $\tau_L$ ) molecular axes [120]. This model has been adopted to successfully describe rotational relaxation of BMIM<sup>+</sup> in BMIMCl IL [119] and [BMIM][BF<sub>4</sub>] ILs [121], and is given by the following equation:

$$R_{1rot}^W(\omega) = A_R [J^W(\omega) + 4J^W(2\omega)], \quad (16)$$

where  $J^W(\omega) = \frac{2}{15} \left[ A_0 \frac{2\tau_1}{1+(\omega\tau_1)^2} + A_1 \frac{2\tau_2}{1+(\omega\tau_2)^2} + A_2 \frac{2\tau_3}{1+(\omega\tau_3)^2} \right]$ ;  $\tau_1 = \tau_S$ ,  $\tau_2 = (1/\tau_S + 1/\tau_L)^{-1}$  and  $\tau_3 = (1/\tau_S + 4/\tau_L)^{-1}$ ; the parameters  $A_0 = (1 - 3\cos^2\alpha)^2/4$ ,  $A_1 = 3\sin^2\alpha/4$  and  $A_2 = 3\sin^4\alpha/4$  are the geometric factors depending on the angle between the  $r$  vector ( $r$  is the intramolecular distance between two nuclei) and the long axis of the molecule,  $\alpha$ . If translational and rotational motions are assumed to be statistically independent and/or dominant in different time scales, the total spin-lattice relaxation rate will be given by:

$$R_{1IL}^{I=1/2}(\omega) = R_{1intra}(\omega) + R_{1inter}(\omega) = R_{1rot}(\omega) + R_{1Diff}^{ii}(\omega) + R_{1Diff}^{ij}(\omega), \quad (17)$$

where homonuclear (ii) and heteronuclear (ij) translational relaxation have been considered. Equation (17) has been used to address the measured relaxation rate dispersions of nuclei with  $I = 1/2$  in ILs in many works [60,101-104,106,108,109,115,116,119].

Most of the studies about ILs with lithium salts that use FFC-NMR relaxometry technique have only focused on relaxation of dipolar nuclei that belong to ions of the IL but a few of them have analyzed the quadrupolar relaxation of <sup>7</sup>Li [60]. The spin-lattice relaxation of nuclei with spin  $I \geq 1$ , such as <sup>7</sup>Li with  $I = 3/2$ , is mainly due to the interaction between the nuclear electric quadrupole, as characterized by its moment  $Q$ , and the fluctuating EFG tensor at the nuclear site, caused by the surrounding intra and intermolecular charge distributions. For a simple Li<sup>+</sup>, the origin of the EFG is intermolecular, and its temporal fluctuations include both long-range translational diffusion and local (short-range) dynamics of Li<sup>+</sup>. In the case of [BMIM]TFSI with LiTFSI, the spin-lattice relaxation rate of lithium was explained by fluctuations of the EFG tensor mostly due to local translational motion of Li<sup>+</sup> within the coordination sphere surrounded by anions [60]. Assuming isotropic diffusional motion given by jumps with an average correlation time  $\tau_{jump}$  as a first approach, a Lorentzian form can express the spin-lattice relaxation rate [60]:

$$R_{1IL}^{Li}(\omega) = A_Q \left[ \frac{\tau_{jump}}{1+(\omega)^2\tau_{jump}^2} + \frac{4\tau_{jump}}{1+(2\omega)^2\tau_{jump}^2} \right], \quad (18)$$

where  $A_Q = \frac{3\pi^2}{10} \frac{(2I+3)}{I^2(2I-1)} \left(1 + \frac{\eta^3}{3}\right)^2 C_Q^2$ ;  $\tau_{jump} \equiv \langle r \rangle^2/6D_s$ ,  $\langle r \rangle^2$  is the average one-jump distance and  $D_s$  is the diffusion coefficient;  $\eta$  is the asymmetry parameter of the EFG and  $C_Q$  is the quadrupolar coupling constant. If an axially symmetric EFG tensor is assumed,  $\eta$  is zero.

MDS are a helpful guide in identifying proper relaxation models since they allow for a determination of diffusion coefficients and rotational correlation times without any further model

assumptions. Therefore, relaxometry experiments and MDS have been combined [115,116] to validate the assumptions made to derive the analytical expressions for the employed relaxation models in ILs. It was demonstrated that nuclear magnetic resonance properties calculated from MDS reproduce measured dispersion curves and temperature trends faithfully [115]. The good agreement between experiment and computation showed that the assumptions made by using, for instance, a Lorentzian model for rotational relaxation are applicable at least in a qualitative way if the ions do not present reorientational dynamics that is substantially anisotropic [116].

#### 4.2. Deep Eutectic Solvents (DESs)

Although NMR spectroscopy is used in the studies of DESs [36,50,52], the use of relaxation times is in their infancy with a few examples to highlight [36,122-126]. Despite this, the following works add to the importance of relaxation times as a valuable tool in ion dynamics studies.

Paterno et.al. [36] studied the  $x\text{AlCl}_3$ :amide DESs series with  $x$  ranging from 1 to 1.7 moles. The amides were of varying alkyl chain length and included: acetamide ( $\text{CH}_3\text{CONH}_2$ ), propionamide ( $\text{CH}_3\text{CH}_2\text{CONH}_2$ ) and butyramide ( $\text{CH}_3\text{CH}_2\text{CH}_2\text{CONH}_2$ ). The objectives of the study were to determine the aluminum ion species interactions and their corresponding dynamics and how both were affected by the amide type. Both  $^1\text{H}$  and  $^{27}\text{Al}$   $T_1$  measurements were determined over the temperature range of 293 – 363 K. The  $^1\text{H}$   $T_1$  data revealed differences in the local environments of the terminal species of each amide. At fixed molar ratios, the  $T_1$  values for the amide ( $\text{NH}_2$ ) group decreased with increasing alkyl chain length, which the authors surmised corresponded with the expected decrease in the dielectric screening ability of the amides. However, unlike the  $\text{NH}_2$  group, at fixed molar ratios the  $^1\text{H}$   $T_1$  for the terminal  $\text{CH}_3$  group was longest and shortest for the propionamide and butyramide DESs respectively. From this result the authors surmised a balancing of the flexibility associated with shorter alkyl chains, and the electrostatic screening afforded by greater dielectric constants provided the most suitable local environment for rotational motion of  $\text{CH}_3$  about its principal  $\text{C}_{3v}$  axis. Additional revelations about the DESs local environments were revealed by the  $^{27}\text{Al}$   $T_1$  data. Firstly, despite it generally having the smallest size and being the most symmetric of the identified aluminum ion species ( $\text{AlCl}_4^-$ ,  $\text{AlCl}_2(\text{amide})^+$ , and  $\text{AlCl}_2(\text{amide})_2^+$ ) in the DESs, the  $\text{AlCl}_4^-$  species experienced the largest EFG as evidenced from it having the shortest  $T_1$  for all amides, at every concentration and temperature. Activation energies determined from the Arrhenius plots of the variable temperature  $T_1$  data also increased for the  $\text{AlCl}_4^-$  species but decreased for the free  $\text{AlCl}_3$  and  $\text{AlCl}_2(\text{amide})^+$  species with increasing molar ratios. The authors surmised that since the local electrostatic interactions would also be stronger for greater  $\text{AlCl}_3$  concentration thereby restricting the species' rotational and translational mobilities, there would be a need for greater activation energies. In contrast to the  $\text{AlCl}_4^-$  species, the  $\text{AlCl}_2(\text{amide})^+$  species dynamics was very dependent on the flexibility of the amides' alkyl chains, with their conformational flexibility effectively reducing the strength of the local EFG the  $\text{AlCl}_2(\text{amide})^+$  species experienced.

Alfurayj et.al [122] studied the effect of different water concentrations (0, 0.1, 1, 10, and 28.5 wt %) on the dynamics of the DES ethaline (a 1:2 mol % mixture of choline chloride and ethylene glycol) by using different experimental techniques, among them NMR diffusometry and broadband relaxometry, and molecular dynamics simulations. The authors showed that translational and rotational motions of choline and ethylene glycol in ethaline accelerated with the presence of water, and the higher the water content, the faster these motions became. This was consistent with decreasing viscosity when water is added. The  $^1\text{H}$  spin-lattice relaxation profiles of choline and ethylene glycol were described by combining the models given by equations (12) and (14).

On the other hand, Fraenza et. al. [124] used these same models to describe the  $^1\text{H}$  spin-lattice relaxation of choline and glycerol in the DES glyceline (a 1:2 mol % mixture of choline chloride and glycerol). The authors combined multiple NMR techniques such as FFC relaxometry, PFG diffusion and  $^{13}\text{C}$  NMR relaxation, to study the dynamics of choline and glycerol as a function of choline chloride concentration (0, 5, 10, 25 and 33mol%). They detected a faster rotational and translational

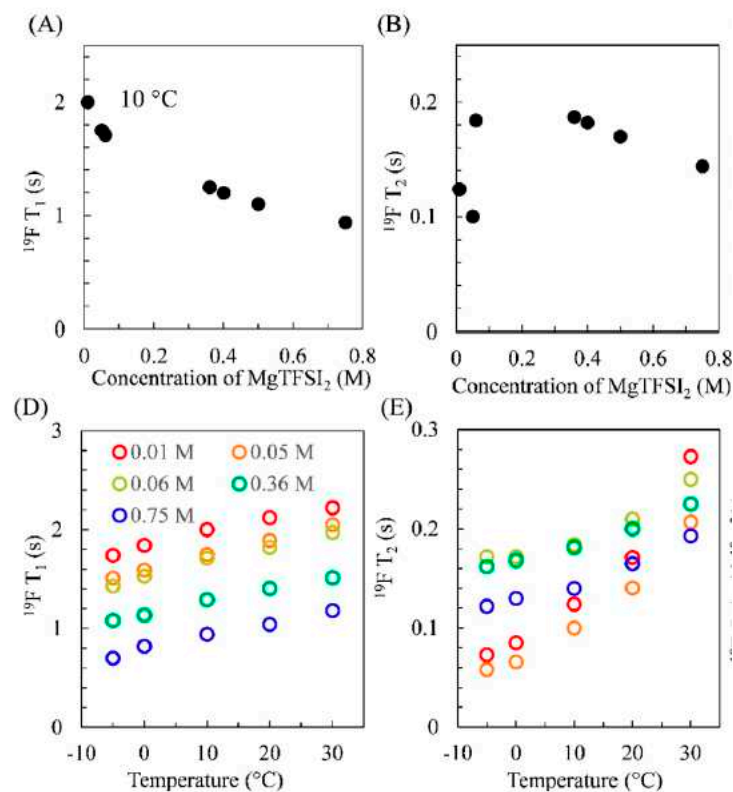
dynamics of all species in glyceline because of the disruption of the glycerol H-bonding network as choline chloride was added, until the eutectic concentration (33mol% choline chloride).

#### 4.3. Organic Solvent Electrolytes

There are numerous relaxation times ( $T_1$ ,  $T_2$ ) studies on organic solvent electrolytes. Although  $\text{Li}^+$  electrolytes have featured most prominently compared to those of other batteries, there have been some studies where relaxation times have provided insight into the ion-ion and ion-solvent interactions, as exist in multivalent ion electrolytes. The following selections highlight the variety of applications of relaxation times.

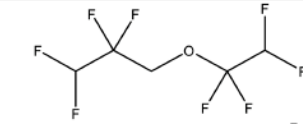
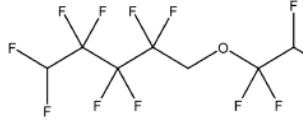
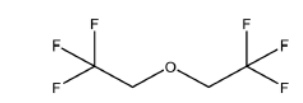
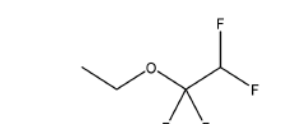
Peng et.al. [127] used  $^{11}\text{B}$   $T_1$  and  $T_2$  measurements to study the  $\text{LiBF}_4$  and  $\text{LiPF}_6$  salts in binary carbonate mixtures comprised of EC and DMC. The  $\text{LiPF}_6$  salt concentration ranged from 0.01 M to 1.2 M, while that for the  $\text{LiBF}_4$  were only 0.01 and 1 M. The EC/DMC solvent compositions used included 80/20, 50/50, 20/80 and 0/100 for both salts. Similar values were obtained for the  $T_1$  and  $T_2$  of the  $\text{LiBF}_4$  mixtures indicating the media were being investigated in the motional narrowing regime. At lower DMC content (ergo higher solvent polarity) the lower salt concentration electrolyte had significantly larger ( $> 10\times$ )  $T_1$  and  $T_2$  values compared to the 1 M electrolyte. However, with increasing DMC content the relaxation values for both electrolytes converged indicating stronger interactions between the anions and cations. Larger ion-ion interactions were observed for the  $\text{LiBF}_4$  electrolytes compared to the  $\text{LiPF}_6$  ones as evidenced by the decreasing  $^{11}\text{B}$  relaxation times. This effect was magnified by increase in DMC concentration, which effectively reduced the overall solvent polarity further enhancing the interactions.

Chen et.al. [128] used  $^{19}\text{F}$   $T_1$  and  $T_2$  measurements in their study of varying concentration of magnesium bis(trifluoromethanesulfonyl) imide ( $\text{MgTFSI}_2$ ) in a 1,2-dimethoxyethane (DME) solvent. This is a common  $\text{Mg}^{2+}$  battery electrolyte but there are questions about its conduction properties. For example, the ionic conductivity reaches a maximum at 0.6 M but decreases until the solution is saturated. Additionally, computational studies suggest that  $\text{MgTFSI}_2$  in DME exists primarily as fully solvated free ions independent of concentration [129,130], which goes against the formation of ion pairs with increasing salt concentration. One argument put forth to explain the saturation behavior is the increase in permittivity caused by the re-dissociation process of contact-ion-pair (CIP) formation at higher concentrations [131]. This process is known to depend on the increase in the orientational polarizability of CIP species at higher concentrations, but the roles of the conformational flexibility of DME and the unbounded anions are undetermined. To elucidate the complexities of this system, the authors did a quantitative analysis of  $\text{Mg}^{2+}$  solvation characteristics with salt concentration as the determining variable.  $^{19}\text{F}$   $T_1$  and  $T_2$  are shown in Figure 1 as functions of both salt concentration (A and B) and temperature (D and E) respectively. The decrease in  $T_1$  correlated with the increase observed in the solution viscosity (not shown) and was associated with a decrease in the rotational dynamics of the  $\text{CF}_3$  groups. The effect of viscosity is evidenced in the  $T_2$  data at higher concentrations ( $\geq 0.36$  M). However, the smaller  $T_2$  values at lower salt concentrations (which corresponded to a drop in self-diffusion coefficient) pointed to the formation of CIP  $\text{Mg}(\text{TFSI})_m(\text{DME})_n$  ( $m, n = 1, 2$ ) structures and the corresponding restricted dynamics. With the aid of  $^{17}\text{O}$  spectra, the authors were able to confirm the structure of the CIP changes with increasing salt concentration, going from  $\text{Mg}(\text{TFSI})(\text{DME})^+$  between 0.01 – 0.05 M,  $\text{Mg}(\text{TFSI})(\text{DME})_2^+$  at 0.06 M, and  $[\text{Mg}(\text{DME})_3]^{2+}$  at higher concentrations.



**Figure 1.**  $^{19}\text{F}$   $T_1$  (A and D) and  $T_2$  (B and E) of  $\text{MgTFSI}_2/\text{DME}$  as a function of salt concentration and temperature. Reproduced/Adapted from Ref. 125 with permission from ACS Publications, Copyright 2020.

Li-Sulfur (Li-S) battery electrolytes often suffer from the complexities of the oxidation and reduction Li-S chemistry and conduction pathways [132-134]. For example, in the conversion of S8 to  $\text{Li}_2\text{S}$ , soluble intermediate lithium polysulfide species ( $\text{Li}_2\text{S}_n$ ,  $n \geq 4$ ) are formed and dissolve into the organic electrolyte resulting in poor Coulombic efficiency and particularly in severe loss of capacity by reacting with Li electrode [135]. One method used to combat the polysulfide dissolution problem, is the implementation of high Li salt concentrations. In these systems, the increase in Li salt concentration increases the CIP formation whereby Li coordination is accomplished by both the salt anion and the solvent molecules. Exceeding the concentration level whereby most solvent molecules are coordinated to Li ions leaves few 'free' solvent molecules available to solubilize the polysulfide species. One system which has been studied in recent years [136-140] is comprised of the  $\text{LiTFSI}$  salt in acetonitrile (MeCN) to form the  $(\text{MeCN})_2\text{-LiTFSI}$  solvate electrolyte. This electrolyte suffers from lower ionic conductivity and correspondingly high viscosity, both of which can be improved using cosolvents such as hydrofluoroether (HFE). Shin et.al. [141] studied the effect of the HFE structure (see Figure 2) on the  $(\text{MeCN})_2\text{-LiTFSI}$  solvate electrolyte using  $^7\text{Li}$   $T_1$  measurements. Values were determined between 238-343 K for the neat and HFE analogues of the  $(\text{MeCN})_2\text{-LiTFSI}$  solvate electrolytes in volume ratios of 2:1, 1:1, and 1:2.

abbreviation	full name	structure
TTE	1,1,2,2-tetrafluoroethyl 2,2,3,3-tetrafluoropropyl ether	
OTE	1H,1H,5H-octafluoropentyl 1,1,2,2-tetrafluoroethyl ether	
BTFE	bis(2,2,2-trifluoroethyl) ether	
ETE	ethyl 1,1,2,2-tetrafluoroethyl ether	

**Figure 2.** Hydrofluoroether cosolvents used for (MeCN)<sub>2</sub>-LiTFSI solvate electrolytes. Reproduced/Adapted from Ref. 138 with permission from ACS Publications, Copyright 2017.

As shown in Figure 3, with increasing HFE content the  $T_1$  minimum shifted to lower temperatures irrespective of the HFE type. This behavior indicates enhancement in the Li<sup>+</sup> mobility caused by the reduced viscosity. The order of the  $T_1$  minimum followed the inverse of the analogue's viscosity. The  $T_1$  minimum also shifted to faster times indicating a more efficient quadrupolar relaxation mechanism, which the authors surmised was the result of increased asymmetry possibly due to the replacement of coordinated MeCN by HFE molecules which have high electron density around the oxygen and fluorine atoms. The fitting of the  $T_1$  data to the BPP model for quadrupolar nuclei (Eq. 19) allowed extraction of  $\tau_c$  and  $\omega_q$ .

$$\frac{1}{T_1} = \frac{\omega_q^2}{50} \left( \frac{\tau_c}{1 + \omega_0^2 \tau_c^2} + \frac{4\tau_c}{1 + 4\omega_0^2 \tau_c^2} \right). \quad (19)$$

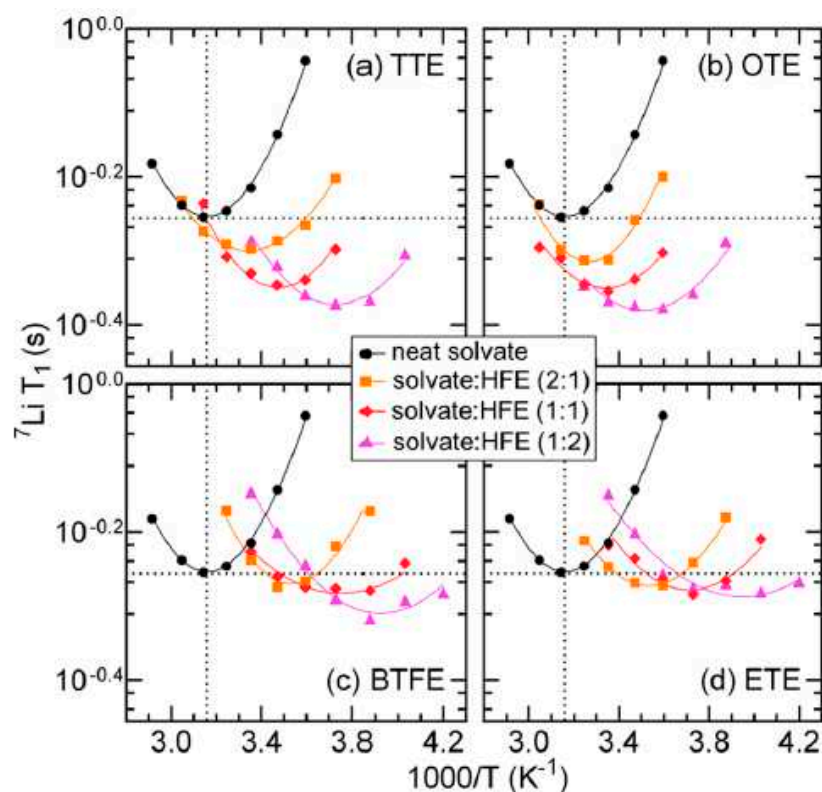


**Figure 3.**  ${}^7\text{Li}$   $T_1$  data for  $(\text{MeCN})_2\text{-LiTFSI}$  solvate electrolytes. Lines represent the fits of the data to the BPP model. Reproduced/Adapted from Ref. 138 with permission from ACS Publications, Copyright 2017.

Here  $\omega_q$  is the quadrupolar coupling constant (QCC), and was found to increase with increasing HFE, suggesting the presence of larger oscillating electric field gradients (EFGs) around the Li ions. Of the HFEs, the TTE and OTE both had larger  $\omega_q$  values which correlated well with their shorter  $T_1$ . This result combined with them having the lower  $\tau_c$  values supported TTE and OTE inducing greater asymmetry compared to BTFE and ETE.

#### 4.4. Confined liquid electrolytes

FFC-NMR relaxometry studies about confined liquid electrolytes have been mostly concentrated on ILs without [103,106,119,121,142-145] and with lithium salt [60], and few of them on aqueous electrolyte solutions [146]. Most of them have been focused on the dynamics of the cation ( ${}^1\text{H}$  NMR) [119,121,142,143,145,146] and only few of them have studied both cation and anion dynamics ( ${}^1\text{H}$  and  ${}^{19}\text{F}$  NMR) [60,103,106,108,144]. Many of these works have shown that the confinement causes a slight slowing-down of the ion dynamics, which is consistent with the fact that the ionic conductivity of the confined electrolyte is usually smaller compared to the corresponding value for the pure IL [119]. However, the opposite effect, this means enhanced ionic conductivity, could be observed depending on the type of confining matrix that is used and how it interacts with ions, since this interaction might prohibit the formation of ion clusters or associates [121,142,146]. For instance, in the following cases enhanced ionic conductivity has been observed: i) the gel electrolyte made of an aqueous solution of tetramethylammonium bromide (TMABr) confined into the low molecular weight organic gelator methyl-4,6-O-(p-nitrobenzylidene)- $\alpha$ -D-glucopyranoside [142,146]; ii) the gel polymer electrolyte based on ethoxylated bisphenol A dimethacrylate and 1-butyl-3-methylimidazolium tetrafluoroborate ( $[\text{BMIM}][\text{BF}_4]$ ) IL [121]. Independently of the type of IL and confining matrix, all of these works [60,103,106,108,119,121,142-144,146] have shown that in the case of the bulk IL electrolyte there is no frequency dependence in the low frequency window (in general below 1 MHz) of the spin-

lattice relaxation rate profiles. Whereas for the confined electrolyte a well-pronounced dispersion is seen in this frequency range, which is a fingerprint of the interactions between the ions and the confining material.

#### 4.4.1. Ionogels (IGs)

The molecular dynamics becomes quite complex when an IL is confined in a mesoporous inorganic matrix as it occurs in an IG. The dynamic properties of ILs in confinement strongly depend on the relative size of the ions and the pores, and on the specific IL and matrix composition. Therefore, two different approaches have been considered to describe the spin-lattice relaxation dispersions of IGs, namely, the two and one ion population approaches.

The two-population approach considers that the size of the pores or cavities of the matrix is big enough to allow the distinction of two ions population, namely, a core fraction, near the pore center and a surface fraction, near the confining walls [103,143,146]. The first one is dominant, and its ions dynamically behave as “bulk-like”. For the second one, the ions interact with the pore walls, and therefore, their dynamics are affected by the matrix surface topology. Other work has identified the bulk-like phase as ions at least a few ionic radii distant from the matrix surfaces and the surface-like phase as those ions close to the matrix surfaces [60]. Then, the total relaxation rate is given by:

$$R_{1IG}^{2\text{ populations}}(\omega) = R_1^{\text{core}}(\omega) + R_1^{\text{surf}}(\omega). \quad (20)$$

Here it is assumed that the residence lifetime of the ions on the surface is longer than the translational correlation time in bulk. In this way, the exchange between the two fractions is slow enough to allow us to distinguish between these two populations, and the contribution to the relaxation from the exchange process can be omitted. Also, weight factors for the two fractions of the liquid can be expressed explicitly by multiplying each term of equation (20) [60]. The spin-lattice relaxation rate of ions that belong to the bulk-like phase ( $R_1^{\text{core}}$ ) is assumed to be given by the equations (17) or (18), depending on the value of the quantum number  $I$  of the nuclei [60,103,143,146]. On the other hand, the relaxation of ions interacting with the confining walls ( $R_1^{\text{surf}}$ ) have been described in two different manners. One of them considers that their dynamics can be represented by the same models of equations (17) or (18) but with a different diffusion constant and rotational correlation time [103,143]. In other words:

$$R_{1IG}^{2\text{ populations}} = R_1^{\text{core}}(\omega) + R_1^{\text{surf}}(\omega) = R_{1\text{Diff}}^{\text{core}}(\omega) + R_{1\text{Rot}}^{\text{core}}(\omega) + R_{1\text{Diff}}^{\text{surf}}(\omega) + R_{1\text{Rot}}^{\text{surf}}(\omega). \quad (21)$$

Here four different dynamic parameters are obtained  $D^{\text{core}}$ ,  $D^{\text{surf}}$ ,  $\tau_{\text{R}}^{\text{core}}$  and  $\tau_{\text{R}}^{\text{surf}}$ . The other manner assumes that the translational displacements of ions become restricted due to the interaction with the confining material, taking different local orientations determined by the topology of the cavity surface. These molecular reorientations mediated by translational displacements (RMTD) of the molecules, which occur on a much slower time scale than bulk rotational or translational diffusion, have been considered as the main relaxation mechanism for ions that interact with the confining walls [60,146]. It is important to notice that the RMTD model can be taken under consideration when the investigated system consists of a polar surface and polar solvents. Then, in this case the total relaxation rate is given by:

$$R_{1IG}^{2\text{ populations}} = R_1^{\text{core}}(\omega) + R_1^{\text{surf}}(\omega) = R_{1\text{Diff}}^{\text{core}}(\omega) + R_{1\text{Rot}}^{\text{core}}(\omega) + R_{1\text{RMTD}}^{\text{surf}}(\omega), \quad (22)$$

where:

$$R_{1\text{RMTD}}^{\text{surf}}(\omega) = A_{\text{RMTD}} [J^{\text{RMTD}}(\omega) + 4J^{\text{RMTD}}(2\omega)]. \quad (23)$$

Here  $A_{\text{RMTD}}$  is a constant that depends on the type of nuclear interaction (dipolar or quadrupolar), on the microstructural features of the confining matrix, on the diffusion coefficient, and on the fraction of molecules at the surface.  $J^{\text{RMTD}}$  can be expressed in terms of modes with wave numbers  $k$  as follows [147]:

$$J^{\text{RMTD}}(\omega) = \frac{1}{(2\pi)^2} \int_0^\infty S(k) \frac{2\tau_k}{1+(\omega\tau_k)^2} dk. \quad (24)$$

$S(k)$  is the orientational structure factor, which represents the geometrical information of the surface in terms of surface modes with wave number  $k$ , and  $\tau_k = \tau_k(k)$ . Both can take different



expressions depending on the assumptions that are made. The motion of ions can be described by two-dimensional diffusion and represented by a Gaussian or Cauchy probability density depending on whether the adsorption is weak or strong, respectively [147]. This determines the expression for  $\tau_k$ . In general, a Gaussian probability density is assumed and in the simplest case  $S(k)$  is considered as a constant [60,146] which is equivalent to the assumption of an equipartition of the wave numbers describing different diffusion modes. In this case,  $R_{1\text{RMTD}}^{\text{surf}}(\omega)$  is given by:

$$R_{1\text{RMTD}}^{\text{surf}}(\omega) = A_{\text{RMTD}} \left[ \omega^{-0.5} \left( f\left(\frac{\omega_{\text{max}}}{\omega}\right) - f\left(\frac{\omega_{\text{min}}}{\omega}\right) \right) + 4(2\omega)^{-0.5} \left( f\left(\frac{\omega_{\text{max}}}{2\omega}\right) - f\left(\frac{\omega_{\text{min}}}{2\omega}\right) \right) \right]. \quad (25)$$

Here  $f(\omega) = \arctan((2\omega)^{0.5} + 1) + \arctan((2\omega)^{0.5} - 1) - \text{arctanh}\left(\frac{(2\omega)^{0.5}}{\omega+1}\right)$ .  $\omega_{\text{min}} = \frac{4D_{\text{surf}}}{l_{\text{max}}^2}$  and  $\omega_{\text{max}} = \frac{4D_{\text{surf}}}{l_{\text{min}}^2}$  represent, respectively, the minimum and maximum frequencies of diffusion modes on the matrix surface;  $D_{\text{surf}}$  denotes the surface diffusion coefficient,  $l_{\text{max}}$  describes the largest, and  $l_{\text{min}}$  describes the smallest displacement distance along the surface. The two-population approach using equations (22) and (25) has been used to successfully describe the spin-lattice relaxation profiles of hydrogen and fluorine in IL electrolytes made of [BMIM][TFSI] with the lithium salt LiTFSI confined in a silica matrix [60]. On the other hand, this model was also applied to describe  $^1\text{H}$  relaxation of an aqueous solution of tetramethylammonium bromide (TMABr) confined into a gel matrix made of a low molecular weight gelator [146].

Another common assumption for  $S(k)$  is that it follows a power law, therefore  $R_{1\text{RMTD}}^{\text{surf}}(\omega)$  is given by [147]:

$$R_{1\text{RMTD}}^{\text{surf}}(\omega) = \widetilde{A_{\text{RMTD}}} \omega^{-p}, \quad 0 < p < 1. \quad (26)$$

The amplitude  $\widetilde{A_{\text{RMTD}}}$  can be written as  $C \times D^{p-1}$ , where  $C$  is a constant that depends on the type of interaction (dipolar or quadrupolar), on the exponent  $p$  and on the type probability density (Gaussian or Cauchy). The temperature dependence is in this case introduced by the diffusion coefficient  $D$ . The two-population approach using equations (18) and (26) was used to depict beyond all expectation  $^7\text{Li}$  relaxation in IGs made of the IL [BMIM][TFSI] with LiTFSI confined into a  $\text{SiO}_2$  matrix [60]. This is a clear indication that RMTD can be as well an efficient relaxation mechanism for quadrupolar nuclei such as  $^7\text{Li}$ .

On the other hand, the one-population approach considers that all ions interact with the confining walls all the time due to the small dimensions of cavities and consequently it is not possible to distinguish two different populations of ions. Under this assumption, the model presented by equation (26) has been used to describe the  $^1\text{H}$  and  $^{19}\text{F}$  spin-lattice relaxation profiles of the IL [BMIM][TFSI] confined in a porous glass [144]. In contrast, the  $^1\text{H}$  and  $^{19}\text{F}$  spin-lattice relaxation profiles of the IL [EMIM][FSI] (1-ethyl-3-methylimidazolium bis(fluorosulfonyl)imide) into a mesoporous MCM41 silica matrix have been explained by two-dimensional (2D) translational diffusion of the ions in the vicinity of the confining walls and rotational motion [106]. The 2D diffusion was considered as a sequence of loops near the confining walls interrupted by time periods during which the ions were attached to the surface. Additionally, the rotational motion of the confined ions was described by two correlation times that were attributed to possible anisotropic reorientation of these species. Therefore, the total relaxation rate in this case was expressed by [106]:

$$R_{1\text{IG}}^{\text{1 population}} = R_1^{2\text{D Diff}}(\omega) + R_1^{\text{Rot,s}}(\omega) + R_1^{\text{Rot,f}}(\omega) + R_1^{\text{FM}}. \quad (27)$$

Here  $R_1^{2\text{D Diff}}(\omega) = A_{\text{trans}} \tau_{\text{trans}} \left[ \ln\left(1 + \frac{1}{(\omega \tau_{\text{trans}})^2}\right) + 4 \ln\left(1 + \frac{1}{(2\omega \tau_{\text{trans}})^2}\right) \right]$ ;  $R_1^{\text{Rot,l}}(\omega)$  follows a Lorentzian form (Eq. (14)) and the superscripts  $l=s, f$  stand for slow and fast rotations. Equation (27) includes a frequency independent term,  $R_1^{\text{FM}}$ , which is associated with dynamical processes being too fast to lead to a visible dependence of the corresponding relaxation contribution on the resonance frequency. It might originate from the internal dynamics of the confined ions.

#### 4.4.1. Gel polymers electrolytes (GPE)

Richardson et.al. [63] used  $T_2$  measurements to illustrate the multiphase complexity of the poly(vinylidene fluoride) (PVDF)/PC/ $\text{LiBF}_4$  polymer gel electrolytes comprised of 20 and 30% PVDF. The

$^1\text{H}$   $T_2$  results revealed a multiphase system comprised of a crystalline PVDF lamellae, an inter lamellae amorphous PVDF, a solvated amorphous PVDF and a liquid electrolyte. Due to the multiphase nature of the electrolytes, a single exponential fitting function as shown in Eq. (4) was not applicable. Instead, the authors used a modified fitting function comprised of the series addition of multiple single exponentials as shown in Eq. (28):

$$M_{x,y} = |M_0^1| e^{-t/T_2^1} + |M_0^2| e^{-t/T_2^2} + |M_0^3| e^{-t/T_2^3}, \quad (28)$$

where  $M_0^1, M_0^2,$  and  $M_0^3$  represent the relative intensity of each phase, and  $T_2^1, T_2^2,$  and  $T_2^3$  are the respective phase's spin-spin relaxation time. Due to the shortness of the  $T_2$  expected for the crystalline PVDF lamellae (microseconds), the authors surmised a three-phase fit was satisfactory for both the 20 and 30% PVDF electrolyte compositions. The intensities determined for the inter lamellae amorphous PVDF, solvated amorphous PVDF and liquid electrolyte phases were 12.7%, 35.7% and 51.6%, and 14%, 42% and 44% for the 20% and 30% PVDF electrolyte compositions respectively. These results were supported by the  $^1\text{H}$  self-diffusion coefficients obtained by standard pulsed field gradient (PFG) measurements.

In the same way as IGs, when the IL is mixed with a polymer gel, the molecular dynamics of the ions become more complex because of the confinement that they experience. They interact with the polymer chains and therefore their translational displacements become restricted taking different local orientations determined by the topology of the polymer network. In recent years a new kind of GPE based on the entrapment of ILs in poly(IL) (PIL) hosts has emerged. One of the main benefits of this type of electrolyte is the prevention of phase separation (sweating out effect) and leakage of the liquid component during application. Recently, a new class of GPE [148-156] comprised of a polymer, a salt, and an IL has gained attention due to its higher ionic conductivity when compared to its gel counterpart [152,153]. Here we discuss a few of these studies.

In an earlier investigation of PIL systems, Gouverneur et.al. [151] used  $^7\text{Li}$   $T_1$  measurements to study the interactions between the polymer-solvent mixture and the  $\text{Li}^+$  ions with specific focus on how the polymer concentration affects dynamics. The PILs studied were comprised of 1-butyl-1-methylpyrrolidinium bis(trifluoromethanesulfonyl) imide (Pyr<sub>14</sub>TFSI), lithium TFSI, and poly(diallyldimethylammonium) TFSI (PDADMATFSI) (see Figure 4a). Samples were comprised of the 20:X:02 and 20:X:04 molar ratios series of IL:PIL:LiTFSI.

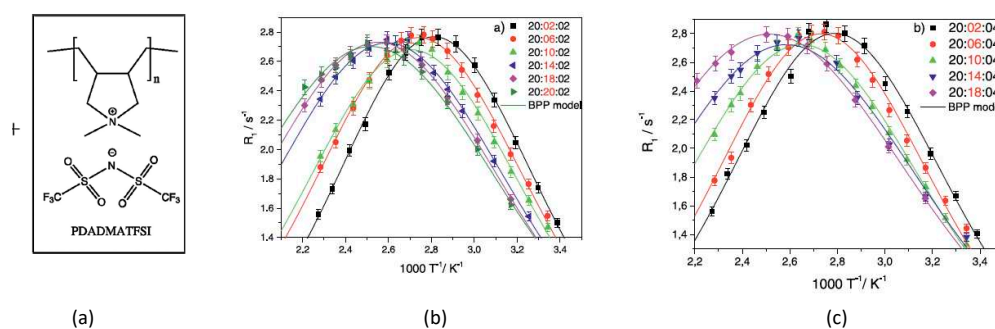


**Figure 4.** (a) PIL structure. Fitting data with BPP model for (b) 20:X:02 and (c) 20:X:04. The solid line represents the BPP equation for  $R_1$  (see Eq. 14). Reproduced/Adapted from Ref. 147 with permission from Elsevier, Copyright 2015.

With increasing PIL concentration the  $R_1$  maximum moves to higher temperatures for both salt concentrations (see Figure 4b and 4c), signifying decreasing  $\text{Li}^+$  dynamics. For each salt concentration, the  $E_A$  values decreased with increasing PIL content despite the reduction in long range dynamics as evidence from both the ionic conductivity and self-diffusion measurements. The authors surmised that the decreasing  $E_A$  values may be due to the PIL's positively charged backbone ergo its ability to break up anion clusters that generally coordinate with  $\text{Li}^+$ . The extracted  $\tau_c$  values increased with

PIL content, suggesting that despite the PIL's aid in breaking up anion clusters, it impedes Li<sup>+</sup> dynamics far more.

On the other side, Brinkkötter et.al. [157] investigated the influence of the polymer on the local dynamics and the local environment of the lithium ion in the same ternary GPE studied by Gouverneur et.al. [151], using frequency and temperature dependent <sup>7</sup>Li T<sub>1</sub> measurements. Even though they obtained the same results as Gouverneur et.al., they discovered that the Cole-Davidson motional model (Eq. (15)), with Arrhenius dependence of the correlation time and a temperature dependent quadrupole coupling constant, described the relaxation rates better than the BPP model did. Additionally, they made a comparison with the GPE based on PEO, and although the local Li<sup>+</sup> motion is reduced by the presence of either polymer, the reduction is less effective in the PDADMA<sup>+</sup> samples. Thus, they concluded that mechanical stabilization of a liquid electrolyte by a polymer can be achieved at a lesser drawback of Li<sup>+</sup> motion when a cationic polymer is used instead of the neutral PEO because the first one induces a fragmentation of lithium-anion clusters, whereas the neutral polymer interacts via a coordination state to the Li<sup>+</sup>.

In a later study, Brinkkötter et.al. [158] used <sup>7</sup>Li T<sub>1</sub> measurements in their determination of the effect of the poly(ionic liquid) (PIL) cationic structure on the physical properties of ternary GPEs. Like Gouverneur et.al. [151] the IL and salt used were Pyr<sub>14</sub>TFSA, and LiTFSA. The PILs used are shown in Figure 5a. The molar ratio of the PIL:IL:LiTFSA system was 4:20:4. In spite of the heterogeneous nature of the materials, all the T<sub>1</sub> data required only a single exponential fitting equation which the authors surmised was due to either the detection of an average value due to fast exchange between the various components, or the fact that the difference between the various T<sub>1</sub> were within the experimental error of the measurements. Over the temperature range (298-423K) studied, the R<sub>1</sub>(1/T<sub>1</sub>) data exhibited a maximum that was sample dependent with that for PIL<sub>1ter</sub> and PIL<sub>2ter</sub> (see Figure 5b) occurring at the lowest and highest temperatures respectively. The authors used the BPP model to extract the τ<sub>c</sub> and activation energies (E<sub>A</sub>) from the Arrhenius fits of the respective T<sub>1</sub> data using the equation:

$$(29) \quad \tau_c = \tau_0 \exp\left(\frac{-E_A}{RT}\right).$$

Here τ<sub>0</sub> is the pre-factor, R is the gas constant and T is the temperature in Kelvin. Contrary to the R<sub>1</sub> maximum location for PIL<sub>1ter</sub> which suggested it had the fastest local ion dynamics of all the composites, it also had the highest E<sub>A</sub> value whereas the PIL<sub>2-4,ter</sub> all had the same value. From this the authors surmised that the PIL<sub>1ter</sub> system had localized connected domains of Pyr<sub>14</sub>TFSA/LiTFSA which were responsible for the enhanced dynamics despite PIL<sub>1</sub> having a higher glass transition temperature and lowest ionic conductivity.

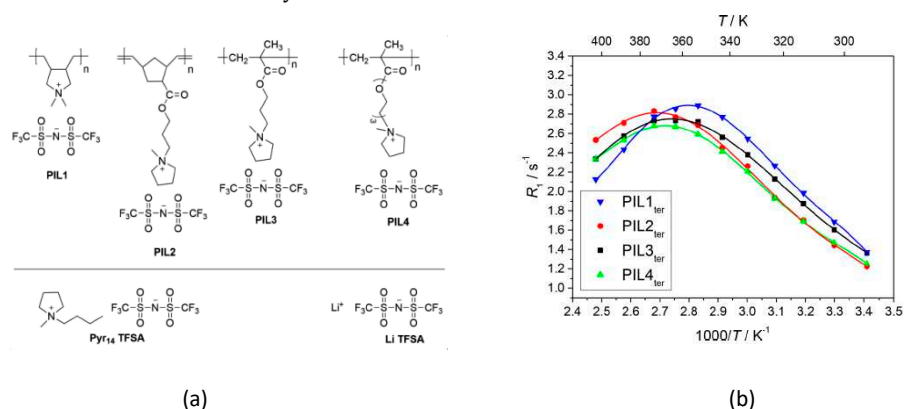


**Figure 5.** (a) Components used for the preparation of the Ternary Gel Electrolyte Systems. (b) Temperature dependent <sup>7</sup>Li R<sub>1</sub> data for the GPEs. Reproduced/Adapted from Ref. 154 with permission from ACS Publications, Copyright 2020.

FFC-NMR relaxometry has also been used to study GPEs, where the confined liquid electrolyte is based on ILs [108,119,121]. In the same way as IGs, the dynamic properties of ILs in confinement strongly depend on the relative size of the ions and the cavities, and on the specific IL and polymer composition. Therefore, the same two different approaches considered for IGs, have been considered as well to describe the spin-lattice relaxation rate dispersions of GPEs (the two and one ion population approaches).

Rachocki et. al. [121] studied BMIM<sup>+</sup> dynamics in the GPE made of [BMIM][BF<sub>4</sub>] and bisphenol A ethoxylate dimethacrylate (bisAEA4) at the mass ratio of 20:80, in the range of temperatures 248-343K. The relaxation of the cation was successfully explained by using the two-population approach given by the model of equation (21). The "bulk-like" fraction was analyzed in terms of translational diffusion using the Torrey's model [117] and local molecular reorientations around a long and a short molecular axis of the IL cation using Woessner's model (Eq. (16)). On the other hand, the fraction of cations interacting with the polymer was described by the RMTD model given by equation (25). Additionally, the authors measured the ionic conductivity through electrochemical impedance spectroscopy, and they observed that its value for GPE was twice higher than that of pure IL. This effect was in agreement with the larger diffusion coefficients obtained from the analysis of the relaxation profiles for the ions interacting with the polymer compared to the corresponding value for the bulk ions. This conductivity enhancement was explained by the interaction of IL aggregates at polymer/IL interface. It was speculated that this interaction leads to a decrease in the size of ion complexes and in the tendency to form ion-pairs or aggregates in the interphase, allowing ions to create new ionic-conducting pathways which can play an important role in ionic conduction observed at the microscopic level. At the same time, BMIM<sup>+</sup> dynamics in the GPE made of BMIMCl and cellulose (Cell) at 10wt% in the range of temperatures 298-368K was studied by Kaszyńska et. al. [119]. The model used to describe the <sup>1</sup>H spin-lattice relaxation rates profiles was the same used by Rachocki et.al. [121]. The conductivity measurements performed for pure IL and that confined in the Cell/BMIMCl GPE showed that the gelation only resulted in a small decrease of the ionic conductivity. This is clear evidence that the type of anion and polymer determine the final properties of GPE because, although both works used the same cation [119,121], the gelation effect on conductivity was different in each case.

Garaga et.al. [108] investigated the cation and anion dynamics in two different GPEs made of the ILs [P<sub>4441</sub>][TFSI] or [N<sub>4441</sub>][TFSI], both with up to 0.6 molal concentration of LiTFSI and the polymethyl methacrylate (PMMA) polymer at 10 wt. %. They measured <sup>1</sup>H and <sup>19</sup>F spin-lattice relaxation rate profiles at different temperatures, which were modeled by considering the one-population approach. RMTD were assumed as the main relaxation mechanism for hydrogen and fluorine in the polymer gels (Eq. (25)), however, a Lorentzian term (Eq. (14)) was added in the case of cation relaxation to consider molecular reorientations that they could experience when they are not interacting with the polymer. This was clear evidence that cations had a less restricted motion than anions under the presence of the polymer which was connected to the more probable interaction between anions and the polymer. In general, the confinement showed a small slow-down in the dynamics of ions.

## 5. Solid Electrolytes

The study of relaxation times in solid materials are generally more challenging compared to liquids. This is because of a number of factors including large quadrupolar coupling, low natural abundance or low resonance frequencies, all of which can affect the data determined, the time required for the measurements, and the data analysis. In spite of these, relaxation times have been used in numerous studies on solid electrolyte materials and the following selections highlights their importance.

As previously stated, PEO is one of the most studied polymers. However, it suffers from low ionic conductivity and mechanical integrity. Several methods have been used to help offset these disadvantages, one of which has been the inclusion of inorganic fillers such as TiO<sub>2</sub> [159], ceramics

[160,161], and lithium-ion conducting ceramic particles such as  $\text{Li}_{1.3}\text{Al}_{0.3}\text{Ti}_{1.7}(\text{PO}_4)_3$  (LATP) [160-163]. In one such study, Peng et.al. [164] studied the effect of the doped LATP filler on the polymer electrolyte (PE) comprised of PEO and the lithium trifluoromethanesulfonate salt ( $\text{LiTf}$ ,  $\text{LiCF}_3\text{SO}_3$ ). The ceramic polymer electrolyte (CPE) contained 55% of the doped LATP (labeled LICGC,  $\text{Li}_2\text{O}-\text{Al}_2\text{O}_3-\text{SiO}_2-\text{P}_2\text{O}_5-\text{TiO}_2-\text{GeO}_2$ ) ceramic and both  $^7\text{Li}$  and  $^{19}\text{F}$   $T_1$  were determined. These results were compared with the ceramic-free polymer electrolyte to ascertain the ceramic's effect on ion dynamics and the interfacial interactions in the polymer-ceramic composite electrolyte. Three Li components were identified in the CPE: the ceramic component, the immobile PE component, and the mobile PE component. Because of the difficulty in resolving the signals, the authors used a biexponential fit for the relaxation profile to determine the values for the ceramic and mobile CPE components:

$$I(\tau) = I_{(0)} \left[ f \left( 1 - 2 \exp \left( \frac{-\tau}{T_1^{\text{LICGC}}} \right) \right) + (1 - f) \left( 1 - 2 \exp \left( \frac{-\tau}{T_1^{\text{mobile Li in PEO}}} \right) \right) \right], \quad (30)$$

where  $I(\tau)$  is the amplitude of the central peak of the  $^7\text{Li}$  spectra at  $\tau$ ,  $f$  is the fraction of Li,  $T_1^{\text{LICGC}}$  represents the  $T_1$  of the ceramic, and  $T_1^{\text{mobile Li in PEO}}$  is the value for the mobile Li in PEO. The immobile component of PE was analyzed from the satellites of the  $^7\text{Li}$  spectra. As shown in Figure 6a, the ceramic hinders both the immobile and mobile Li components as evidenced by the reduced  $T_1$  values of the CPE compared to the PE. It should be pointed out that the  $^7\text{Li}$   $T_1$  values for the LICGC pristine and in CPE were identical, indicating that the quadrupolar environment in both were similar. The  $^{19}\text{F}$  data for all species showed  $T_1$  minimum (see Figure 6b). That for the mobile F occurred around 40°C which was lower than that for the mobile Li. The authors attributed this difference to the fast rotation of the  $\text{CF}_3$  group around the C-S bond. As expected, the  $T_1$  for the mobile F was shorter in the CPE than in PE. In spite of the reduced mobility of both ions, the ceramic's presence in the PE caused an increase in the  $\text{Li}^+$  transference number indicating greater immobilization for anions than cations.

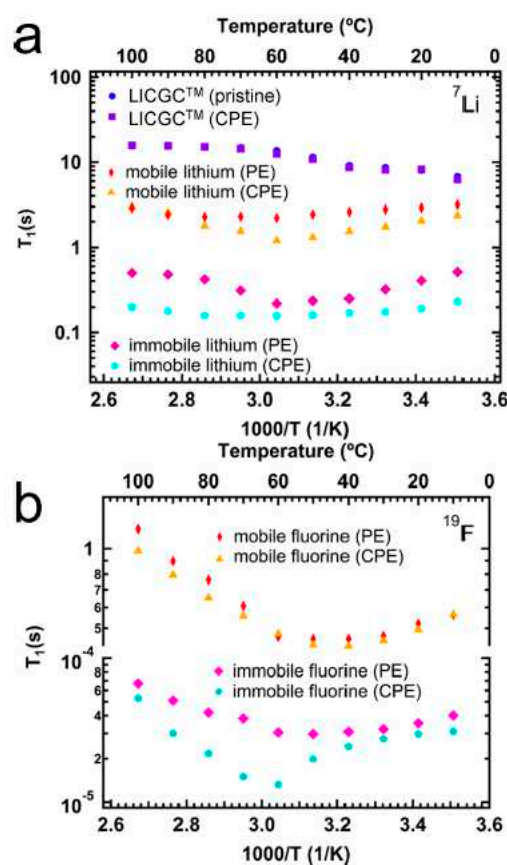


**Figure 6.** (a)  ${}^7\text{Li}$  and (b)  ${}^{19}\text{F}$   $T_1$  data of LICGC, PE and CPE as a function of inverse temperature. Reproduced/Adapted from Ref. 160 with permission from ACS Publications, Copyright 2020. .

The similarities between Li and sodium (Na) ions have contributed to the synthesis and investigation of Na ion electrolytes like Li ones [165-169]. Pope et.al. [169] used  ${}^{23}\text{Na}$  spectra and  $T_1$  to study SPE based on the poly(2-acrylamido-2-methyl-1-propane-sulfonic acid) (PAMPS) monomer,  $\text{Na}^+$  and dimethylbutylmethoxyethyl ammonium ( $\text{N}_{114(201)}$ ) cations in the 2:8 molar ratio (see Figure 7a and 7b). The authors objectives included a direct comparison of the  $\text{Na}^+$  ion transport with that of  $\text{Li}^+$  in the lithium analogue electrolyte, and the determination of the ether group's role in the  $\text{Na}^+$  solvation and subsequent dissociation. As shown in Figure 7c, two distinct environments were discerned from the bi-exponentially fitting of the  $T_1$  data. The shorter  $T_1$  component was assigned to the mobile  $\text{Na}^+$  cations while the longer  $T_1$  component was due to the immobile or bound  $\text{Na}^+$  cations associated with the sulfonate groups. Evidence of increasing segmental dynamics is visible from the dramatic decrease in values of the immobile  $\text{Na}^+$  cations above the glass transition temperature ( $T_g$ ) with increasing temperature, in particular between 323 – 333K.

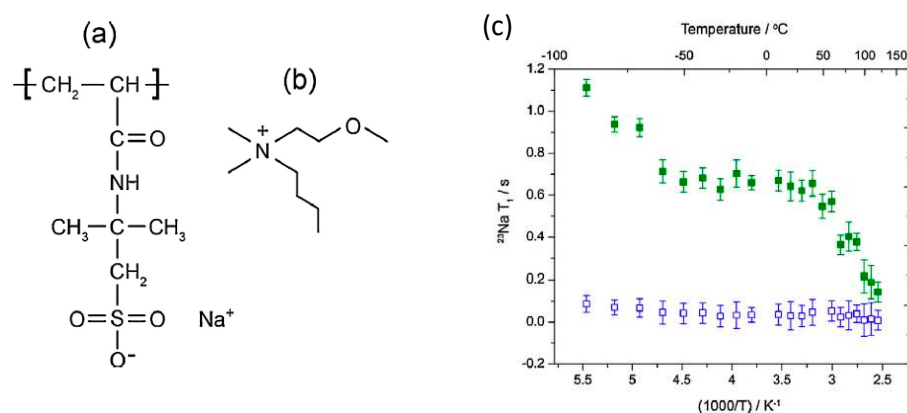


**Figure 7.** (a) Structure of the ionomer, (b) the poly(2-acrylamido-2-methyl-1-propane-sulfonic acid) (PAMPS) monomer, and (c)  ${}^{23}\text{Na}$   $T_1$  data. Reproduced/Adapted from Ref. 165 with permission from Elsevier, Copyright 2015.

One of the most studied solid electrolyte is the NASICON (sodium (Na) Super Ionic CONductor) family [170-173], with structure  $\text{Na}_{3+x}\text{Sc}_2(\text{SiO}_4)_x(\text{PO}_4)_{3-x}$  (see Figure 8). Like most solid electrolytes, this family suffers from low room temperature ionic conductivity. The highest conductivity value observed at 298K is  $6.9 \times 10^{-4}$  S/cm obtained for the  $x = 4$  electrolyte [174]. Zinkevich et.al. [173] used multi-nuclear ( ${}^{23}\text{Na}$ ,  ${}^{31}\text{P}$  and  ${}^{45}\text{Sc}$ ) spectra and relaxometry studies to investigate the sodium ion dynamics at the microscopic scale. The temperature dependent  ${}^{23}\text{Na}$   $R_1$  ( $1/T_1$ ) data for  $x = 0.1 - 0.8$  all showed a maximum that occurred at higher temperatures with increasing  $x$ . Due to the difference in slopes between the high and low temperature sides of each BPP modeled v-shaped curve, the authors surmised the existence of correlated motions.

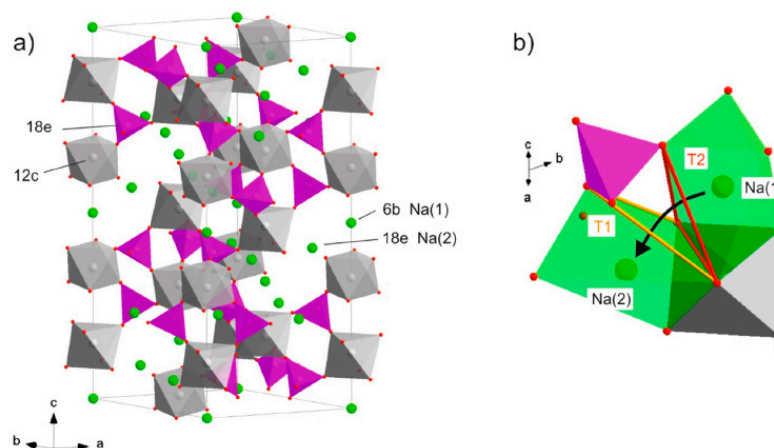


**Figure 8.** (a) The rhombohedral crystal structure of  $\text{Na}_{3+x}\text{Sc}_2(\text{SiO}_4)_x(\text{PO}_4)_{3-x}$  with space group R3c. (b) the jump of  $\text{Na}^+$  ions between Na(1) and Na(2) sites through the oxygen triangles  $T_1$  and  $T_2$ . Reproduced/Adapted from Ref. 166 with permission from Elsevier, Copyright 2020. .

The authors used the Arrhenius relationship for a thermally activated process (Eq. (31)) to determine the  $E_A$  values.

$$\tau_c(T) = \tau_{298\text{ K}} \exp\left(\frac{E_A}{k_B} \left(\frac{1}{T} - \frac{1}{298\text{ K}}\right)\right).$$

(31)

Here  $\tau_{298\text{ K}}$  is the correlation time at room temperature, and  $T$  is the temperature. The  $E_A$  values determined decreased with increasing  $x$  ergo increasing Si content. The authors attributed this effect to the expansion of the unit cell volume which allows the transport of  $\text{Na}^+$ . However, this process is also impeded by the increasing concentration of  $\text{Na}^+$ , which reduces the vacancy number thereby lowering the ionic conductivity.

Lithium and sodium doped solid glass electrolytes have gained attention for solid-state applications [175-179]. This is because of the decoupling of the ionic conduction from the media's structural relaxation and the possibility of its tuning to provide the favored properties. One method of tuning is through the combination of multiple glass formers. These mixed-glass former oftentimes experience non-linear changes in the materials' electrical, thermal, mechanical and chemical properties. Both positive and negative non-linear changes are possible and are referred to as the mixed glass former effect (MGFE). In dynamic's characterization of these materials' NMR spectra and  $T_1$  measurements has been invaluable by providing correlation times and activation energies that differ from those obtained by dc conductivity measurements. These deviations have been instrumental in the realization of the decoupling between the ionic conduction and structural relaxation pathways. The following results are examples of the invaluable information gleaned from  $T_1$  determination.

Storek et.al. [177] used  $^{23}\text{Na}$  spectra and  $T_1$  measurements in their comparison of ion dynamics in two glasses –  $0.33\text{Na}_2\text{O} + 0.67[x\text{B}_2\text{O}_3 + (1-x)2\text{SiO}_2]$  with a known negative MGFE, and  $0.35\text{Na}_2\text{O} + 0.65[x\text{B}_2\text{O}_3 + (1-x)\text{P}_2\text{O}_5]$  with a known positive MGFE. In the case of the negative MGFE electrolyte, the  $R_1$  ( $1/T_1$ ) results decreased with increasing  $x\text{B}_2\text{O}_3$  concentration and displayed a minimum between 0.6 – 0.8 indicative of slow ion dynamics. By comparison, the positive MGFE electrolyte showed an increasing  $R_1$  with a maximum at  $x \cong 0.4$  over the temperature range studied. Activation energies determined were larger than those from both dc conductivity and tracer diffusion measurements and were explained using a percolation model.

In their study of the ternary glass family of electrolytes of the form  $y\text{Na}_2\text{S} + (1-y)[x\text{SiS}_2 + (1-x)\text{PS}_{5/2}]$ , Shastri et.al. [179] used  $^{23}\text{Na}$   $T_1$  to determine the distribution of activation energies around the sodium ions due from the heterogeneous nature of the materials. These distributions correlated

with a mean barrier height for the sodium ion hopping motion facilitated by the dominant quadrupolar interaction. Unlike the Storek study [177], no pronounced MGFE was observed, however the activation energy barrier height decreased with increasing SiS<sub>2</sub> concentration. Additionally, the authors determined through their use of the Anderson-Stuart model [176,180] that the activation energy was the sum of the Coulombic contribution due to the mobile sodium ions interacting with other ions in the glass, and a strain contribution caused by the cations' displacement of other ions during their motions. They also determined that the energy barriers were strongly dependent on the materials' dielectric constants.

The use of FFC-NMR relaxometry to study solid electrolytes is quite scarce basically because of two reasons. On one side, the short value of the  $T_2$  makes the signal measurement unfeasible and on the other side, even when it is possible to measure the signal, the values of  $T_1$  at low magnetic fields in general are shorter or in the same range than the switching time (2-3 ms). This makes  $T_1$  measurement unachievable due to electronic limitations. However, a few works using FFC-NMR to investigate solid electrolytes such as glasses [175], glass ceramics [181], and polymer electrolytes [182] have been reported.

Gabriel et. al. [175], used <sup>7</sup>Li FFC-NMR to study the ionic jump motion and to determine the distribution of activation energies in the ternary 0.5Li<sub>2</sub>S+0.5[(1-x)GeS<sub>2</sub>+xGeO<sub>2</sub>] glass system with x = 0 (reference) and 0.1 (higher conductivity), at different temperatures in the range 200-450K. Two models were employed and compared to explain the <sup>7</sup>Li  $T_1$  rate profiles, namely, the multi-exponential (ME) autocorrelation function model and the power-law waiting time model. For the first one, the relaxation rate was described by a superposition of Lorentzian functions with a distribution of the correlation times,  $C(\tau_c)$ , as follows:

$$R_{1glass\_ME}^{Li}(\omega) = A_Q \left[ \int_0^\infty C(\tau_c) \frac{\tau_c}{(1+\omega^2\tau_c^2)} d\tau_c + \int_0^\infty C(\tau_c) \frac{4\tau_c}{(1+(2\omega)^2\tau_c^2)} d\tau_c \right]. \quad (32)$$

Here  $C(\tau_c)$  was specified by assuming thermally activated ion hops that follow an Arrhenius relation and a temperature-independent Gaussian distribution  $g(E_A)$  for the activation energy:

$$g(E_A) = \frac{1}{\sigma\sqrt{2\pi}} e^{-\frac{(E_A-\langle E_A \rangle)^2}{2\sigma^2}}. \quad (33)$$

This model described the data very well for temperatures higher than 300K, which indicated a change in the <sup>7</sup>Li  $T_1$  mechanism upon cooling. On the other hand, in order to take into account other origins of the non-exponential relaxation, the power-law waiting time model was considered. It comes from the theory of a random walk in a random potential energy landscape and considers a random variation of barrier heights on the length scale of individual ion positions in the glass network [183,184]. Thus, this model leads to a spectral density of the Cole-Cole (CC) type and the relaxation rate in this case is given by:

$$R_{1glass\_CC}^{Li}(\omega) = A_Q \left[ \frac{4\omega^{\alpha-1}\tau_{CC}^\alpha \sin(\alpha\pi/2)}{4+4(\omega\tau_{CC})^\alpha \cos(\frac{\alpha\pi}{2})+(\omega\tau_{CC})^{2\alpha}} + \frac{16\omega^{\alpha-1}\tau_{CC}^\alpha \sin(\alpha\pi/2)}{4+4(2\omega\tau_{CC})^\alpha \cos(\frac{\alpha\pi}{2})+(2\omega\tau_{CC})^{2\alpha}} \right], \quad (34)$$

where there is a single time parameter  $\tau_c$ , in contrast to distribution  $C(\tau_c)$  considered in the ME model, and a non-exponentiality of the dynamical process is introduced and controlled via the width parameter  $\alpha$ . This model also well described the <sup>7</sup>Li data, therefore it was not possible for the authors to determine which model was more accurate based on their data.

Besides, Haaks et. al. [181] investigated Li<sup>+</sup> dynamics in 70Li<sub>2</sub>S-30P<sub>2</sub>S<sub>5</sub> glass electrolyte (LiPS-GL) and glass-ceramic (LiPS-GC) obtained from this glass after heat treatment at 553K for 1h. They used <sup>7</sup>Li  $T_1$  as well as static field gradient NMR to characterize short-range ion jumps and long-range ion diffusion, respectively. In spite of the fact that, in general, ceramization involves controlled crystallization and produces materials featuring both amorphous and crystalline phases, none of the <sup>7</sup>Li NMR approaches yielded evidence for bimodal Li<sup>+</sup> dynamics for LiPS-GC. Their results showed that ceramization substantially enhances the Li<sup>+</sup> mobility on all length scales. They concluded that the correlation functions in LiPS-GC are strongly nonexponential and they used the same ME approach considered by Gabriel et. al. [175] to describe the <sup>7</sup>Li  $T_1$  profiles (Eq. (32)).



The polymer electrolyte made of unentangled poly(propylene glycol) (PPG) and lithium perchlorate ( $\text{LiClO}_4$ ) or LiTFSI has been investigated by Becher et. al. [182] They used  $^1\text{H}$  and  $^7\text{Li}$   $T_1$  measurements as a function of frequency at salts concentrations of 15:1 and 6:1 (ratio of polymer oxygens to lithium ions) in order to study the polymer and  $\text{Li}^+$  dynamics, respectively, in the wide range of temperatures of 290-380K. The  $R_1$  profiles of the polymer were successfully described by assuming that segmental motion at short times ( $R_{1CD}(\omega)$ ) was followed by Rouse dynamics at longer times ( $R_{1Rouse}(\omega)$ ), omitting further intermolecular (translational) contributions. Thus, the total relaxation rate was depicted by a weighted superposition of these two mechanisms:

$$R_1^{Polymer}(\omega) = R_{1CD}(\omega) + R_{1Rouse}(\omega). \quad (35)$$

The segmental motion was treated in the framework of glassy dynamics and the related spectral density showed the CD form (Eq. (15)). On the other side, the contribution associated with Rouse dynamics was given by [185]:

$$R_{1Rouse}(\omega) = A_{DD}\tau_o \left[ \sum_{p,q=1}^{N-1} \frac{p^2+q^2}{(p^2+q^2)^2+(\omega\tau_o N^2)^2} + 4 \sum_{p,q=1}^{N-1} \frac{p^2+q^2}{(p^2+q^2)^2+(2\omega\tau_o N^2)^2} \right], \quad (36)$$

where  $N$  denotes the number of Rouse beads and  $\tau_o$  is a time constant, which is proportional to the friction coefficient of the Rouse model reduced. Concerning polymer segmental motion, the addition of salts leads to not only an increase of correlation times but also of dynamical heterogeneity. Even bimodal dynamical behavior was observed for 15:1 salt concentration, which was explained by the coexistence of salt-rich and salt-depleted regions in these samples. For this concentration, the authors described the  $^1\text{H}$  relaxation dispersion by a superposition of two CD functions. On the other hand, they concluded that there was a strong coupling of polymer and  $\text{Li}^+$  dynamics and therefore described the  $^7\text{Li}$  relaxation profiles using the same model given by Eq. (35). Interestingly, bimodal dynamics was not observed for  $\text{Li}^+$  which suggested that the vast majority of  $\text{Li}^+$  accumulate in salt-rich domains, whereas a very minor fraction resides in salt-depleted domains so that, unlike for the polymer segmental motion, different  $\text{Li}^+$  dynamics in the latter regions remain unobserved.

## 6. Conclusions

In the last few decades researchers have focused on the development and improvement of electrolyte materials. In spite of the increasing complexities of materials' design, through stimuli such as temperature, materials composition and concentration, relaxometry measurements have revealed how the various ions interactions affect the electrolytes' dynamics. Studies of solute particles in ionic liquids have demonstrated the dissimilarities between the polar and non-polar local environments. Relaxometry has provided evidence of the fully solvated free ion nature of  $\text{Mg}^{2+}$  irrespective of concentration in the MgTFSI/DME electrolyte. Moreover, it has revealed the existence of two different ion populations ("bulk-like" and "wall-interacting" fractions) in specific types of confined IL electrolytes. In spite of the stronger interactions associated with solid electrolytes, relaxometry has provided evidence of the multiple ionic environments (i.e., mobile vs. immobile) that exist, as well as the dissimilarities between their cationic and anionic dynamics. Finally, relaxometry results have shown that ceramization substantially enhances the  $\text{Li}^+$  mobility in glass-ceramic electrolytes. The results from all these studies are clear evidence of the potentiality of NMR relaxometry to study dynamics in electrolytes for energy storage.

## 7. Acknowledgements

SS was supported by the National Science Foundation, Solid State and Materials Chemistry Program, Division of Materials Research, EAGER award # 1841398 and RAPID award # 2034643. CF and SG (Hunter College) acknowledge support from Breakthrough Electrolytes for Energy Storage (BEES), an Energy Frontier Research Center funded by the U.S. Department of Energy, Office of Science, Basic Energy Sciences (BES), under award # DESC0019409.

## 8. Abbreviations

BF <sub>4</sub>	Tetrafluoroborate
BMS	Battery Management System
BPP	Bloemburgen, Purcell, and Pound
C <sub>2</sub> C <sub>1</sub> im	1-ethyl-3-methylimidazolium (also called EMIM)
C <sub>4</sub> C <sub>1</sub> im	1-butyl-3-methylimidazolium (also called BMIM)
C <sub>8</sub> C <sub>1</sub> im	1-methyl-3-octylimidazolium
CD	Cole-Davidson
CF <sub>3</sub> SO <sub>2</sub> ) <sub>2</sub> N <sup>-</sup>	Bis(trifluoromethylsulfonyl)amide (also called TFSI, TFSA)
CIP	Contact-ion-pair
DEC	Diethyl carbonate
DMC	Dimethyl carbonate
DES	Deep eutectic solvents
EC	Ethylene carbonate
EDLC	Electric double layer capacitor
EFG	Electric field gradient
FEC	Fluoroethylene carbonate
FFC	Fast field cycling
FFHS	Force-free-hard-sphere
FSI	Bis(fluorosulfonyl)imide (also called FSA, FSI)
GPE	Gel polymer electrolytes
IL	Ionic Liquid
IG	Ionogel
LEDC	Lithium ethylene decarbonates
LIB	Lithium-ion battery
LiBF <sub>4</sub>	Lithium tetrafluoroborate
LiClO <sub>4</sub>	Lithium perchlorate
LiCF <sub>3</sub> SO <sub>3</sub>	Lithium trifluoromethanesulfonate
MDS	Molecular dynamics simulations
NTf <sub>2</sub>	bis(trifluoromethanesulfonyl)imide (also called TFSA, TFSI)
PC	Propylene carbonate
PF <sub>6</sub>	Hexafluorophosphate
PEFC	Polymer electrolyte fuel cell
PEO	Poly (ethylene oxide)
PVDF	Poly (vinylidene fluoride)
QCC	Quadrupolar coupling constant
RMTD	Reorientations mediated by translational displacements
SEI	Solid electrolyte interface
SED	Stokes-Einstein-Debye
SOFC	Solid oxide fuel cell
SPE	Solid polymer electrolytes

TEP	Triethyl phosphate
TMP	Trimethyl phosphate
VC	Vinylene carbonate

## References

- Vangari, M.; Pryor, T.; Jiang, L. Supercapacitors: review of materials and fabrication methods. *Journal of energy engineering* **2013**, *139*, 72-79.
- Zhong, C.; Deng, Y.; Hu, W.; Qiao, J.; Zhang, L.; Zhang, J. A review of electrolyte materials and compositions for electrochemical supercapacitors. *Chemical Society Reviews* **2015**, *44*, 7484-7539.
- Zang, X.; Shen, C.; Sanghadasa, M.; Lin, L. High-voltage supercapacitors based on aqueous electrolytes. *ChemElectroChem* **2019**, *6*, 976-988.
- Conti, J.; Holtberg, P.; Diefenderfer, J.; LaRose, A.; Turnure, J.T.; Westfall, L. *International energy outlook 2016 with projections to 2040*; USDOE Energy Information Administration (EIA), Washington, DC (United States ...: 2016.
- Hansen, K.; Breyer, C.; Lund, H. Status and perspectives on 100% renewable energy systems. *Energy* **2019**, *175*, 471-480.
- Cantarero, M.M.V. Of renewable energy, energy democracy, and sustainable development: A roadmap to accelerate the energy transition in developing countries. *Energy Research & Social Science* **2020**, *70*, 101716.
- Iqbal, M.Z.; Siddique, S.; Hussain, G.; Iqbal, M.W. Room temperature spin valve effect in the NiFe/Gr-hBN/Co magnetic tunnel junction. *Journal of Materials Chemistry C* **2016**, *4*, 8711-8715.
- Blomgren, G.E. The development and future of lithium ion batteries. *Journal of The Electrochemical Society* **2016**, *164*, A5019.
- Placke, T.; Kloepsch, R.; Dühnen, S.; Winter, M. Lithium ion, lithium metal, and alternative rechargeable battery technologies: the odyssey for high energy density. *Journal of Solid State Electrochemistry* **2017**, *21*, 1939-1964.
- Zubi, G.; Dufo-López, R.; Carvalho, M.; Pasaoglu, G. The lithium-ion battery: State of the art and future perspectives. *Renewable and Sustainable Energy Reviews* **2018**, *89*, 292-308.
- Ding, Y.; Cano, Z.P.; Yu, A.; Lu, J.; Chen, Z. Automotive Li-ion batteries: current status and future perspectives. *Electrochemical Energy Reviews* **2019**, *2*, 1-28.
- Miller, J.R.; Simon, P. Electrochemical capacitors for energy management. *science* **2008**, *321*, 651-652.
- Stoller, M.D.; Park, S.; Zhu, Y.; An, J.; Ruoff, R.S. Graphene-based ultracapacitors. *Nano letters* **2008**, *8*, 3498-3502.
- Wang, Y.; Shi, Z.; Huang, Y.; Ma, Y.; Wang, C.; Chen, M.; Chen, Y. Supercapacitor devices based on graphene materials. *The Journal of Physical Chemistry C* **2009**, *113*, 13103-13107.
- Wu, H.; He, D.; Wang, Y.; Fu, M.; Liu, Z.; Wang, J.; Wang, H. Graphene as the electrode material in supercapacitors. In *Proceedings of the 2010 8th International Vacuum Electron Sources Conference and Nanocarbon, 2010*; pp. 465-466.
- Ervin, M.H.; Miller, B.S.; Hanrahan, B.; Maily, B.; Palacios, T. A comparison of single-wall carbon nanotube electrochemical capacitor electrode fabrication methods. *Electrochimica acta* **2012**, *65*, 37-43.
- Pope, M.A.; Korkut, S.; Punckt, C.; Aksay, I.A. Supercapacitor electrodes produced through evaporative consolidation of graphene oxide-water-ionic liquid gels. *Journal of the Electrochemical Society* **2013**, *160*, A1653.
- Feng, X.; Ouyang, M.; Liu, X.; Lu, L.; Xia, Y.; He, X. Thermal runaway mechanism of lithium ion battery for electric vehicles: A review. *Energy Storage Materials* **2018**, *10*, 246-267.
- Deng, K.; Zeng, Q.; Wang, D.; Liu, Z.; Qiu, Z.; Zhang, Y.; Xiao, M.; Meng, Y. Single-ion conducting gel polymer electrolytes: design, preparation and application. *Journal of Materials Chemistry A* **2020**, *8*, 1557-1577.
- Aurbach, D.; Zaban, A.; Schechter, A.; Ein-Eli, Y.; Zinigrad, E.; Markovsky, B. The study of electrolyte solutions based on ethylene and diethyl carbonates for rechargeable Li batteries: I. Li metal anodes. *Journal of The Electrochemical Society* **1995**, *142*, 2873.
- Xu, K.; Lam, Y.; Zhang, S.S.; Jow, T.R.; Curtis, T.B. Solvation sheath of Li<sup>+</sup> in nonaqueous electrolytes and its implication of graphite/electrolyte interface chemistry. *The Journal of Physical Chemistry C* **2007**, *111*, 7411-7421.
- Shi, S.; Lu, P.; Liu, Z.; Qi, Y.; Hector Jr, L.G.; Li, H.; Harris, S.J. Direct calculation of Li-ion transport in the solid electrolyte interphase. *Journal of the American Chemical Society* **2012**, *134*, 15476-15487.
- Shi, S.; Qi, Y.; Li, H.; Hector Jr, L.G. Defect thermodynamics and diffusion mechanisms in Li<sub>2</sub>CO<sub>3</sub> and implications for the solid electrolyte interphase in Li-ion batteries. *The Journal of Physical Chemistry C* **2013**, *117*, 8579-8593.

24. Philippe, B.; Dedryvère, R.m.; Gorgoi, M.; Rensmo, H.k.; Gonbeau, D.; Edström, K. Role of the LiPF<sub>6</sub> salt for the long-term stability of silicon electrodes in Li-ion batteries—A photoelectron spectroscopy study. *Chemistry of Materials* **2013**, *25*, 394-404.
25. Seo, D.M.; Chalasani, D.; Parimalam, B.S.; Kadam, R.; Nie, M.; Lucht, B.L. Reduction reactions of carbonate solvents for lithium ion batteries. *ECS Electrochemistry Letters* **2014**, *3*, A91.
26. Yoon, T.; Milien, M.S.; Parimalam, B.S.; Lucht, B.L. Thermal decomposition of the solid electrolyte interphase (SEI) on silicon electrodes for lithium ion batteries. *Chemistry of Materials* **2017**, *29*, 3237-3245.
27. Parimalam, B.S.; MacIntosh, A.D.; Kadam, R.; Lucht, B.L. Decomposition reactions of anode solid electrolyte interphase (SEI) components with LiPF<sub>6</sub>. *The Journal of Physical Chemistry C* **2017**, *121*, 22733-22738.
28. Rezaqita, A.; Kathribail, A.-R.; Kahr, J.; Jahn, M. Analysis of degradation of Si/Carbon || LiNi<sub>0.5</sub>Mn<sub>0.3</sub>Co<sub>0.2</sub>O<sub>2</sub> full cells: effect of prelithiation. *Journal of The Electrochemical Society* **2019**, *166*, A5483.
29. Etacheri, V.; Marom, R.; Elazari, R.; Salitra, G.; Aurbach, D. Challenges in the development of advanced Li-ion batteries: a review. *Energy & Environmental Science* **2011**, *4*, 3243-3262.
30. Ponrouch, A.; Marchante, E.; Courty, M.; Tarascon, J.-M.; Palacin, M.R. In search of an optimized electrolyte for Na-ion batteries. *Energy & Environmental Science* **2012**, *5*, 8572-8583.
31. Bhide, A.; Hofmann, J.; Dürr, A.K.; Janek, J.; Adelhelm, P. Electrochemical stability of non-aqueous electrolytes for sodium-ion batteries and their compatibility with Na<sub>0.7</sub>CoO<sub>2</sub>. *Physical Chemistry Chemical Physics* **2014**, *16*, 1987-1998.
32. Shakourian-Fard, M.; Kamath, G.; Smith, K.; Xiong, H.; Sankaranarayanan, S.K. Trends in Na-ion solvation with alkyl-carbonate electrolytes for sodium-ion batteries: insights from first-principles calculations. *The Journal of Physical Chemistry C* **2015**, *119*, 22747-22759.
33. Cresce, A.V.; Russell, S.M.; Borodin, O.; Allen, J.A.; Schroeder, M.A.; Dai, M.; Peng, J.; Gobet, M.P.; Greenbaum, S.G.; Rogers, R.E. Solvation behavior of carbonate-based electrolytes in sodium ion batteries. *Physical Chemistry Chemical Physics* **2017**, *19*, 574-586.
34. Xing, L.; Zheng, X.; Schroeder, M.; Alvarado, J.; von Wald Cresce, A.; Xu, K.; Li, Q.; Li, W. Deciphering the ethylene carbonate-propylene carbonate mystery in Li-ion batteries. *Accounts of chemical research* **2018**, *51*, 282-289.
35. Li, K.; Zhang, J.; Lin, D.; Wang, D.-W.; Li, B.; Lv, W.; Sun, S.; He, Y.-B.; Kang, F.; Yang, Q.-H. Evolution of the electrochemical interface in sodium ion batteries with ether electrolytes. *Nature communications* **2019**, *10*, 725.
36. Paterno, D.; Rock, E.; Forbes, A.; Iqbal, R.; Mohammad, N.; Suarez, S. Aluminum ions speciation and transport in acidic deep eutectic AlCl<sub>3</sub> amide electrolytes. *Journal of Molecular Liquids* **2020**, *319*, 114118.
37. Paterno, D.; Suarez, S. Aluminum Ion Species Transport in Pure and Additive Modulated Deep Eutectic Solvents (DES) Electrolytes. *ECS Transactions* **2020**, *98*, 401.
38. Rumble, C.A.; Kaintz, A.; Yadav, S.K.; Conway, B.; Araque, J.C.; Baker, G.A.; Margulis, C.; Maroncelli, M. Rotational dynamics in ionic liquids from NMR relaxation experiments and simulations: Benzene and 1-ethyl-3-methylimidazolium. *The Journal of Physical Chemistry B* **2016**, *120*, 9450-9467.
39. Lo Celso, F.; Appetecchi, G.B.; Simonetti, E.; Zhao, M.; Castner Jr, E.W.; Keiderling, U.; Gontrani, L.; Triolo, A.; Russina, O. Microscopic structural and dynamic features in triphilic room temperature ionic liquids. *Frontiers in chemistry* **2019**, *7*, 285.
40. Zhao, M.; Wu, B.; Lall-Ramnarine, S.I.; Ramdihal, J.D.; Papacostas, K.A.; Fernandez, E.D.; Sumner, R.A.; Margulis, C.J.; Wishart, J.F.; Castner Jr, E.W. Structural analysis of ionic liquids with symmetric and asymmetric fluorinated anions. *The Journal of chemical physics* **2019**, *151*, 074504.
41. Suarez, S.N.; Rúa, A.; Cuffari, D.; Pilar, K.; Hatcher, J.L.; Ramati, S.; Wishart, J.F. Do TFSA anions slither? Pressure exposes the role of TFSA conformational exchange in self-diffusion. *The Journal of Physical Chemistry B* **2015**, *119*, 14756-14765.
42. Yoshimura, Y.; Shigemi, M.; Takaku, M.; Yamamura, M.; Takekiyo, T.; Abe, H.; Hamaya, N.; Wakabayashi, D.; Nishida, K.; Funamori, N. Stability of the liquid state of imidazolium-based ionic liquids under high pressure at room temperature. *The Journal of Physical Chemistry B* **2015**, *119*, 8146-8153.
43. Harris, K.R.; Kanakubo, M. Self-diffusion, velocity cross-correlation, distinct diffusion and resistance coefficients of the ionic liquid [BMIM][Tf<sub>2</sub>N] at high pressure. *Physical Chemistry Chemical Physics* **2015**, *17*, 23977-23993.
44. Nazet, A.; Sokolov, S.; Sonnleitner, T.; Makino, T.; Kanakubo, M.; Buchner, R. Densities, viscosities, and conductivities of the imidazolium ionic liquids [Emim][Ac],[Emim][FAP],[Bmim][BETI],[Bmim][FSI],[Hmim][TFSI], and [Omim][TFSI]. *Journal of Chemical & Engineering Data* **2015**, *60*, 2400-2411.
45. Pilar, K.; Rua, A.; Suarez, S.N.; Mallia, C.; Lai, S.; Jayakody, J.; Hatcher, J.L.; Wishart, J.F.; Greenbaum, S. Investigation of dynamics in BMIM TFSA ionic liquid through variable temperature and pressure NMR relaxometry and diffusometry. *Journal of the Electrochemical Society* **2017**, *164*, H5189.

46. Shimizu, K.; Freitas, A.A.; Lopes, J.N.C. Structural characterization of the [CnCl<sub>m</sub>][C<sub>4</sub>F<sub>9</sub>SO<sub>3</sub>] ionic liquid series: alkyl versus perfluoroalkyl side chains. *Journal of Molecular Liquids* **2017**, *226*, 28-34.
47. Brooks, N.J.; Castiglione, F.; Doherty, C.M.; Dolan, A.; Hill, A.J.; Hunt, P.A.; Matthews, R.P.; Mauri, M.; Mele, A.; Simonutti, R. Linking the structures, free volumes, and properties of ionic liquid mixtures. *Chemical science* **2017**, *8*, 6359-6374.
48. Harris, K.R.; Kanakubo, M.; Kodama, D.; Makino, T.; Mizuguchi, Y.; Watanabe, M.; Watanabe, T. Temperature and density dependence of the transport properties of the ionic liquid triethylpentylphosphonium bis (trifluoromethanesulfonyl) amide, [P<sup>222</sup>, 5][Tf<sub>2</sub>N]. *Journal of Chemical & Engineering Data* **2018**, *63*, 2015-2027.
49. Bagh, F.S.G.; Shahbaz, K.; Mjalli, F.S.; Hashim, M.A.; AlNashef, I.M. Zinc (II) chloride-based deep eutectic solvents for application as electrolytes: preparation and characterization. *Journal of Molecular Liquids* **2015**, *204*, 76-83.
50. Hu, P.; Zhang, R.; Meng, X.; Liu, H.; Xu, C.; Liu, Z. Structural and spectroscopic characterizations of amide-AlCl<sub>3</sub>-based ionic liquid analogues. *Inorganic chemistry* **2016**, *55*, 2374-2380.
51. Zhang, Y.; Han, J.; Liao, C. Insights into the properties of deep eutectic solvent based on reline for Ga-controllable CIGS solar cell in one-step electrodeposition. *Journal of The Electrochemical Society* **2016**, *163*, D689.
52. Angell, M.; Pan, C.-J.; Rong, Y.; Yuan, C.; Lin, M.-C.; Hwang, B.-J.; Dai, H. High Coulombic efficiency aluminum-ion battery using an AlCl<sub>3</sub>-urea ionic liquid analog electrolyte. *Proceedings of the National Academy of Sciences* **2017**, *114*, 834-839.
53. Liu, C.; Chen, W.; Wu, Z.; Gao, B.; Hu, X.; Shi, Z.; Wang, Z. Density, viscosity and electrical conductivity of AlCl<sub>3</sub>-amide ionic liquid analogues. *Journal of Molecular Liquids* **2017**, *247*, 57-63.
54. Tome, L.I.; Baiao, V.; da Silva, W.; Brett, C.M. Deep eutectic solvents for the production and application of new materials. *Applied Materials Today* **2018**, *10*, 30-50.
55. Garaga, M.N.; Persson, M.; Yaghini, N.; Martinelli, A. Local coordination and dynamics of a protic ammonium based ionic liquid immobilized in nano-porous silica micro-particles probed by Raman and NMR spectroscopy. *Soft matter* **2016**, *12*, 2583-2592.
56. Guyomard-Lack, A.; Said, B.; Dupré, N.; Galarneau, A.; Le Bideau, J. Enhancement of lithium transport by controlling the mesoporosity of silica monoliths filled by ionic liquids. *New Journal of Chemistry* **2016**, *40*, 4269-4276.
57. Garaga, M.N.; Aguilera, L.; Yaghini, N.; Matic, A.; Persson, M.; Martinelli, A. Achieving enhanced ionic mobility in nanoporous silica by controlled surface interactions. *Physical Chemistry Chemical Physics* **2017**, *19*, 5727-5736.
58. Ashby, D.S.; DeBlock, R.H.; Lai, C.-H.; Choi, C.S.; Dunn, B.S. Patternable, solution-processed ionogels for thin-film lithium-ion electrolytes. *Joule* **2017**, *1*, 344-358.
59. Chen, N.; Zhang, H.; Li, L.; Chen, R.; Guo, S. Ionogel electrolytes for high-performance lithium batteries: A review. *Advanced Energy Materials* **2018**, *8*, 1702675.
60. Jayakody, N.K.; Fraenza, C.C.; Greenbaum, S.G.; Ashby, D.; Dunn, B.S. NMR relaxometry and diffusometry analysis of dynamics in ionic liquids and ionogels for use in lithium-ion batteries. *The Journal of Physical Chemistry B* **2020**, *124*, 6843-6856.
61. Liang, S.; Yan, W.; Wu, X.; Zhang, Y.; Zhu, Y.; Wang, H.; Wu, Y. Gel polymer electrolytes for lithium ion batteries: Fabrication, characterization and performance. *Solid State Ionics* **2018**, *318*, 2-18.
62. Cheng, X.; Pan, J.; Zhao, Y.; Liao, M.; Peng, H. Gel polymer electrolytes for electrochemical energy storage. *Advanced Energy Materials* **2018**, *8*, 1702184.
63. Richardson, P.; Voice, A.; Ward, I. NMR self diffusion and relaxation time measurements for poly (vinylidene fluoride)(PVDF) based polymer gel electrolytes containing LiBF<sub>4</sub> and propylene carbonate. *Polymer* **2016**, *97*, 69-79.
64. Woo, H.-S.; Son, H.; Min, J.-Y.; Rhee, J.; Lee, H.-T.; Kim, D.-W. Ionic liquid-based gel polymer electrolyte containing zwitterion for lithium-oxygen batteries. *Electrochimica Acta* **2020**, *345*, 136248.
65. Tikekar, M.D.; Archer, L.A.; Koch, D.L. Stabilizing electrodeposition in elastic solid electrolytes containing immobilized anions. *Science advances* **2016**, *2*, e1600320.
66. Yue, L.; Ma, J.; Zhang, J.; Zhao, J.; Dong, S.; Liu, Z.; Cui, G.; Chen, L. All solid-state polymer electrolytes for high-performance lithium ion batteries. *Energy Storage Materials* **2016**, *5*, 139-164.
67. Mauger, A.; Armand, M.; Julien, C.; Zaghbi, K. Challenges and issues facing lithium metal for solid-state rechargeable batteries. *Journal of Power Sources* **2017**, *353*, 333-342.
68. Famprikis, T.; Canepa, P.; Dawson, J.A.; Islam, M.S.; Masquelier, C. Fundamentals of inorganic solid-state electrolytes for batteries. *Nature materials* **2019**, *18*, 1278-1291.
69. Kato, Y.; Hori, S.; Saito, T.; Suzuki, K.; Hirayama, M.; Mitsui, A.; Yonemura, M.; Iba, H.; Kanno, R. High-power all-solid-state batteries using sulfide superionic conductors. *Nature Energy* **2016**, *1*, 1-7.

70. Wang, W.; Fang, Z.; Zhao, M.; Peng, Y.; Zhang, J.; Guan, S. Solid polymer electrolytes based on the composite of PEO–LiFSI and organic ionic plastic crystal. *Chemical Physics Letters* **2020**, *747*, 137335.
71. Cai, D.; Wang, D.; Chen, Y.; Zhang, S.; Wang, X.; Xia, X.; Tu, J. A highly ion-conductive three-dimensional LLZAO-PEO/LiTFSI solid electrolyte for high-performance solid-state batteries. *Chemical Engineering Journal* **2020**, *394*, 124993.
72. Sengwa, R.; Dhatarwal, P. Predominantly chain segmental relaxation dependent ionic conductivity of multiphase semicrystalline PVDF/PEO/LiClO<sub>4</sub> solid polymer electrolytes. *Electrochimica Acta* **2020**, *338*, 135890.
73. Zhou, Q.; Li, Q.; Liu, S.; Yin, X.; Huang, B.; Sheng, M. High Li-ion conductive composite polymer electrolytes for all-solid-state Li-metal batteries. *Journal of Power Sources* **2021**, *482*, 228929.
74. Polu, A.R.; Singh, P.K. Improved ion dissociation and amorphous region of PEO based solid polymer electrolyte by incorporating tetracyanoethylene. *Materials Today: Proceedings* **2022**, *49*, 3093-3097.
75. Ngai, K.S.; Ramesh, S.; Ramesh, K.; Juan, J.C. A review of polymer electrolytes: fundamental, approaches and applications. *Ionics* **2016**, *22*, 1259-1279.
76. Mindemark, J.; Lacey, M.J.; Bowden, T.; Brandell, D. Beyond PEO—Alternative host materials for Li<sup>+</sup>-conducting solid polymer electrolytes. *Progress in Polymer Science* **2018**, *81*, 114-143.
77. Xue, Z.; He, D.; Xie, X. Poly (ethylene oxide)-based electrolytes for lithium-ion batteries. *Journal of Materials Chemistry A* **2015**, *3*, 19218-19253.
78. Brooks, D.J.; Merinov, B.V.; Goddard III, W.A.; Kozinsky, B.; Mailoa, J. Atomistic description of ionic diffusion in PEO–LiTFSI: Effect of temperature, molecular weight, and ionic concentration. *Macromolecules* **2018**, *51*, 8987-8995.
79. Mongcopa, K.I.S.; Tyagi, M.; Mailoa, J.P.; Samsonidze, G.; Kozinsky, B.; Mullin, S.A.; Gribble, D.A.; Watanabe, H.; Balsara, N.P. Relationship between segmental dynamics measured by quasi-elastic neutron scattering and conductivity in polymer electrolytes. *ACS Macro Letters* **2018**, *7*, 504-508.
80. Chen, F.; Pringle, J.M.; Forsyth, M. Insights into the transport of alkali metal ions doped into a plastic crystal electrolyte. *Chemistry of Materials* **2015**, *27*, 2666-2672.
81. Lin, D.; Liu, W.; Liu, Y.; Lee, H.R.; Hsu, P.-C.; Liu, K.; Cui, Y. High ionic conductivity of composite solid polymer electrolyte via in situ synthesis of monodispersed SiO<sub>2</sub> nanospheres in poly (ethylene oxide). *Nano letters* **2016**, *16*, 459-465.
82. Fu, X.; Liu, Y.; Wang, W.; Han, L.; Yang, J.; Ge, M.; Yao, Y.; Liu, H. Probing the fast lithium-ion transport in small-molecule solid polymer electrolytes by solid-state NMR. *Macromolecules* **2020**, *53*, 10078-10085.
83. Wang, Q.; Liu, X.; Cui, Z.; Shangguan, X.; Zhang, H.; Zhang, J.; Tang, K.; Li, L.; Zhou, X.; Cui, G. A fluorinated polycarbonate based all solid state polymer electrolyte for lithium metal batteries. *Electrochimica Acta* **2020**, *337*, 135843.
84. Abragam, A. *The principles of nuclear magnetism*; Oxford university press: 1961.
85. Mason, J. *Multinuclear NMR*; Plenum Press: 1987.
86. Slichter, C.P. *Principles of Magnetic Resonance*; Springer Verlag: 1996; Volume 1.
87. Kimmich, R. *NMR: tomography, diffusometry, relaxometry*; Springer-Verlag: 1997.
88. Kowalewski, J.; Maler, L. *Nuclear spin relaxation in liquids: theory, experiments, and applications*; CRC press: 2006.
89. Levitt, M.H. *Spin dynamics: Basics of Nuclear Magnetic Resonance* John Wiley & Sons. *New York-London-Sydney* **2008**.
90. Price, W.S. *NMR studies of translational motion: principles and applications*; Cambridge University Press: 2009.
91. Bloembergen, N.; Purcell, E.M.; Pound, R.V. Relaxation effects in nuclear magnetic resonance absorption. *Physical review* **1948**, *73*, 679.
92. Chiappe, C.; Sanzone, A.; Mendola, D.; Castiglione, F.; Famulari, A.; Raos, G.; Mele, A. Pyrazolium-versus imidazolium-based ionic liquids: structure, dynamics and physicochemical properties. *The Journal of Physical Chemistry B* **2013**, *117*, 668-676.
93. Castiglione, F.; Famulari, A.; Raos, G.; Meille, S.V.; Mele, A.; Appetecchi, G.B.; Passerini, S. Pyrrolidinium-based ionic liquids doped with lithium salts: how does Li<sup>+</sup> coordination affect its diffusivity? *The Journal of Physical Chemistry B* **2014**, *118*, 13679-13688.
94. Khatun, S.; Castner Jr, E.W. Ionic liquid–solute interactions studied by 2D NOE NMR spectroscopy. *The Journal of Physical Chemistry B* **2015**, *119*, 9225-9235.
95. Di Pietro, M.E.; Castiglione, F.; Mele, A. Anions as dynamic probes for ionic liquid mixtures. *The Journal of Physical Chemistry B* **2020**, *124*, 2879-2891.
96. Yasaka, Y.; Kimura, Y. Polarity and nonpolarity of ionic liquids viewed from the rotational dynamics of carbon monoxide. *The Journal of Physical Chemistry B* **2015**, *119*, 15493-15501.
97. Endo, T.; Sumida, H.; Fujii, K.; Takahashi, K.; Kimura, Y. Heterogeneous Structures of Ionic Liquids as Probed by CO Rotation with Nuclear Magnetic Resonance Relaxation Analysis and Molecular Dynamics Simulations. *The Journal of Physical Chemistry B* **2020**, *124*, 10465-10476.

98. Strate, A.; Neumann, J.; Overbeck, V.; Bónsa, A.-M.; Michalik, D.; Paschek, D.; Ludwig, R. Rotational and translational dynamics and their relation to hydrogen bond lifetimes in an ionic liquid by means of NMR relaxation time experiments and molecular dynamics simulation. *The Journal of chemical physics* **2018**, *148*, 193843.
99. Kimmich, R.; Ansaldo, E. Field-cycling NMR relaxometry. *Progress in Nuclear Magnetic Resonance Spectroscopy* **2004**, *44*, 257-320, doi:<https://doi.org/10.1016/j.pnmrs.2004.03.002>.
100. Kimmich, R. *Field-cycling NMR Relaxometry: Instrumentation, Model Theories and Applications*; Royal Society of Chemistry: 2018.
101. Kruk, D.; Meier, R.; Rachocki, A.; Korpała, A.; Singh, R.; Rössler, E. Determining diffusion coefficients of ionic liquids by means of field cycling nuclear magnetic resonance relaxometry. *The Journal of Chemical Physics* **2014**, *140*, 244509.
102. Seyedlar, A.O.; Stapf, S.; Mattea, C. Dynamics of the ionic liquid 1-butyl-3-methylimidazolium bis(trifluoromethylsulphonyl) imide studied by nuclear magnetic resonance dispersion and diffusion. *Physical Chemistry Chemical Physics* **2015**, *17*, 1653-1659.
103. Kruk, D.; Wojciechowski, M.; Brym, S.; Singh, R.K. Dynamics of ionic liquids in bulk and in confinement by means of <sup>1</sup>H NMR relaxometry—BMIM-OcSO<sub>4</sub> in an SiO<sub>2</sub> matrix as an example. *Physical Chemistry Chemical Physics* **2016**, *18*, 23184-23194.
104. Wencka, M.; Apih, T.; Korošec, R.C.; Jencyk, J.; Jarek, M.; Szutkowski, K.; Jurga, S.; Dolinšek, J. Molecular dynamics of 1-ethyl-3-methylimidazolium triflate ionic liquid studied by <sup>1</sup>H and <sup>19</sup>F nuclear magnetic resonances. *Physical Chemistry Chemical Physics* **2017**, *19*, 15368-15376.
105. Beira, M.; Daniel, C.I.; Almeida, P.L.; Corvo, M.C.; Rosatella, A.A.; Afonso, C.A.; Sebastião, P.J. <sup>1</sup>H NMR Relaxometry and Diffusometry Study of Magnetic and Nonmagnetic Ionic Liquid-Based Solutions: Cosolvent and Temperature Effects. *The Journal of Physical Chemistry B* **2017**, *121*, 11472-11484.
106. Kruk, D.; Wojciechowski, M.; Florek-Wojciechowska, M.; Singh, R.K. Dynamics of Ionic Liquids in Confinement by Means of NMR Relaxometry—EMIM-FSI in a Silica Matrix as an Example. *Materials* **2020**, *13*, 4351.
107. Overbeck, V.; Schröder, H.; Bónsa, A.-M.; Neymeyr, K.; Ludwig, R. Insights into the translational and rotational dynamics of cations and anions in protic ionic liquids by means of NMR fast-field-cycling relaxometry. *Physical Chemistry Chemical Physics* **2021**, *23*, 2663-2675.
108. Garaga, M.N.; Jayakody, N.; Fraenza, C.C.; Itin, B.; Greenbaum, S. Molecular-level insights into structure and dynamics in ionic liquids and polymer gel electrolytes. *Journal of Molecular Liquids* **2021**, *329*, 115454.
109. Overbeck, V.; Appelhagen, A.; Rössler, R.; Niemann, T.; Ludwig, R. Rotational correlation times, diffusion coefficients and quadrupolar peaks of the protic ionic liquid ethylammonium nitrate by means of <sup>1</sup>H fast field cycling NMR relaxometry. *Journal of Molecular Liquids* **2021**, *322*, 114983.
110. Kruk, D.; Masiewicz, E.; Lotarska, S.; Markiewicz, R.; Jurga, S. Relationship between Translational and Rotational Dynamics of Alkyltriethylammonium-Based Ionic Liquids. *International Journal of Molecular Sciences* **2022**, *23*, 1688.
111. Silva, G.M.; Beira, M.J.; Morgado, P.; Branco, L.C.; Sebastião, P.J.; Lopes, J.N.C.; Filipe, E.J. Ionic liquids with hydrogenated and perfluorinated chains: Structural study of the [P6, 6, 6, 14][FnCOO]<sup>n-</sup> n= 7, 9, 11. Checking the existence of polar-hydrogenated-perfluorinated triphilic continuity. *Journal of Molecular Liquids* **2022**, *367*, 120506.
112. Hwang, L.P.; Freed, J.H. Dynamic effects of pair correlation functions on spin relaxation by translational diffusion in liquids. *The Journal of Chemical Physics* **1975**, *63*, 4017-4025.
113. Ayant, Y.; Belorizky, E.; Aluzon, J.; Gallice, J. Calcul des densités spectrales résultant d'un mouvement aléatoire de translation en relaxation par interaction dipolaire magnétique dans les liquides. *Journal de Physique* **1975**, *36*, 991-1004.
114. Sholl, C. Nuclear spin relaxation by translational diffusion in liquids and solids: high-and low-frequency limits. *Journal of Physics C: Solid State Physics* **1981**, *14*, 447.
115. Honegger, P.; Overbeck, V.; Strate, A.; Appelhagen, A.; Sappl, M.; Heid, E.; Schröder, C.; Ludwig, R.; Steinhäuser, O. Understanding the nature of nuclear magnetic resonance relaxation by means of fast-field-cycling relaxometry and molecular dynamics simulations—the validity of relaxation models. *The journal of physical chemistry letters* **2020**, *11*, 2165-2170.
116. Overbeck, V.; Golub, B.; Schroeder, H.; Appelhagen, A.; Paschek, D.; Neymeyr, K.; Ludwig, R. Probing relaxation models by means of Fast Field-Cycling relaxometry, NMR spectroscopy and molecular dynamics simulations: Detailed insight into the translational and rotational dynamics of a protic ionic liquid. *Journal of Molecular Liquids* **2020**, *319*, 114207.
117. Torrey, H.C. Nuclear spin relaxation by translational diffusion. *Physical Review* **1953**, *92*, 962.
118. Freed, J.H. Dynamic effects of pair correlation functions on spin relaxation by translational diffusion in liquids. II. Finite jumps and independent T<sub>1</sub> processes. *The Journal of Chemical Physics* **1978**, *68*, 4034-4037.

119. Kaszyńska, J.; Rachocki, A.; Bielejewski, M.; Tritt-Goc, J. Influence of cellulose gel matrix on BMIMCl ionic liquid dynamics and conductivity. *Cellulose* **2017**, *24*, 1641-1655.
120. Woessner, D. Spin relaxation processes in a two-proton system undergoing anisotropic reorientation. *The Journal of Chemical Physics* **1962**, *36*, 1-4.
121. Rachocki, A.; Andrzejewska, E.; Dembna, A.; Tritt-Goc, J. Translational dynamics of ionic liquid imidazolium cations at solid/liquid interface in gel polymer electrolyte. *European Polymer Journal* **2015**, *71*, 210-220.
122. Alfurayj, I.; Fraenza, C.C.; Zhang, Y.; Pandian, R.; Spittle, S.; Hansen, B.; Dean, W.; Gurkan, B.; Savinell, R.; Greenbaum, S. Solvation Dynamics of Wet Ethaline: Water is the Magic Component. *The Journal of Physical Chemistry B* **2021**.
123. Triolo, A.; Di Pietro, M.E.; Mele, A.; Lo Celso, F.; Brehm, M.; Di Lisio, V.; Martinelli, A.; Chater, P.; Russina, O. Liquid structure and dynamics in the choline acetate: urea 1: 2 deep eutectic solvent. *The Journal of Chemical Physics* **2021**, *154*, 244501.
124. Fraenza, C.C.; Elgammal, R.A.; Garaga, M.N.; Bhattacharyya, S.; Zawodzinski, T.A.; Greenbaum, S.G. Dynamics of glycine and interactions of constituents: A multitechnique NMR study. *The Journal of Physical Chemistry B* **2022**, *126*, 890-905.
125. de Araujo Lima e Souza, G.; Di Pietro, M.E.; Castiglione, F.; Vanoli, V.; Mele, A. Insights into the Effect of Lithium Doping on the Deep Eutectic Solvent Choline Chloride: Urea. *Materials* **2022**, *15*, 7459.
126. Di Pietro, M.E.; Goloviznina, K.; van den Bruinhorst, A.; de Araujo Lima e Souza, G.; Costa Gomes, M.; Padua, A.A.; Mele, A. Lithium Salt Effects on the Liquid Structure of Choline Chloride-Urea Deep Eutectic Solvent. *ACS Sustainable Chemistry & Engineering* **2022**, *10*, 11835-11845.
127. Peng, J.; Gobet, M.; Devany, M.; Xu, K.; von Wald Cresce, A.; Borodin, O.; Greenbaum, S. Multinuclear magnetic resonance investigation of cation-anion and anion-solvent interactions in carbonate electrolytes. *Journal of Power Sources* **2018**, *399*, 215-222.
128. Chen, Y.; Jaegers, N.R.; Wang, H.; Han, K.S.; Hu, J.Z.; Mueller, K.T.; Murugesan, V. Role of Solvent Rearrangement on Mg<sup>2+</sup> Solvation Structures in Dimethoxyethane Solutions using Multimodal NMR Analysis. *The Journal of Physical Chemistry Letters* **2020**, *11*, 6443-6449.
129. Salama, M.; Shterenberg, I.; Gizbar, H.; Eliaz, N.N.; Kosa, M.; Keinan-Adamsky, K.; Afri, M.; Shimon, L.J.; Gottlieb, H.E.; Major, D.T. Unique behavior of dimethoxyethane (DME)/Mg (N(SO<sub>2</sub>CF<sub>3</sub>)<sub>2</sub>)<sub>2</sub> solutions. *The Journal of Physical Chemistry C* **2016**, *120*, 19586-19594.
130. Kubisiak, P.; Eilmes, A. Solvation of Mg<sup>2+</sup> Ions in Mg (TFSI)<sub>2</sub>-dimethoxyethane electrolytes—a view from molecular dynamics simulations. *The Journal of Physical Chemistry C* **2018**, *122*, 12615-12622.
131. Self, J.; Hahn, N.T.; Fong, K.D.; McClary, S.A.; Zavadil, K.R.; Persson, K.A. Ion pairing and redissociation in low-permittivity electrolytes for multivalent battery applications. *The journal of physical chemistry letters* **2020**, *11*, 2046-2052.
132. Patel, M.U.; Demir-Cakan, R.; Morcrette, M.; Tarascon, J.M.; Gaberscek, M.; Dominko, R. Li-S Battery Analyzed by UV/Vis in Operando Mode. *ChemSusChem* **2013**, *6*, 1177-1181.
133. Lowe, M.A.; Gao, J.; Abreuña, H.D. Mechanistic insights into operational lithium-sulfur batteries by in situ X-ray diffraction and absorption spectroscopy. *Rsc Advances* **2014**, *4*, 18347-18353.
134. See, K.A.; Leskes, M.; Griffin, J.M.; Britto, S.; Matthews, P.D.; Emly, A.; Van der Ven, A.; Wright, D.S.; Morris, A.J.; Grey, C.P. Ab initio structure search and in situ <sup>7</sup>Li NMR studies of discharge products in the Li-S battery system. *Journal of the American Chemical Society* **2014**, *136*, 16368-16377.
135. Su, Y.-S.; Fu, Y.; Cochell, T.; Manthiram, A. A strategic approach to recharging lithium-sulphur batteries for long cycle life. *Nature communications* **2013**, *4*, 2985.
136. Cuisinier, M.; Cabelguen, P.-E.; Adams, B.; Garsuch, A.; Balasubramanian, M.; Nazar, L. Unique behaviour of nonsolvents for polysulphides in lithium-sulphur batteries. *Energy & Environmental Science* **2014**, *7*, 2697-2705.
137. Yamada, Y.; Furukawa, K.; Sodeyama, K.; Kikuchi, K.; Yaegashi, M.; Tateyama, Y.; Yamada, A. Unusual stability of acetonitrile-based superconcentrated electrolytes for fast-charging lithium-ion batteries. *Journal of the American Chemical Society* **2014**, *136*, 5039-5046.
138. See, K.A.; Wu, H.-L.; Lau, K.C.; Shin, M.; Cheng, L.; Balasubramanian, M.; Gallagher, K.G.; Curtiss, L.A.; Gewirth, A.A. Effect of hydrofluoroether cosolvent addition on Li solvation in acetonitrile-based solvate electrolytes and its influence on S reduction in a Li-S battery. *ACS applied materials & interfaces* **2016**, *8*, 34360-34371.
139. Cheng, L.; Curtiss, L.A.; Zavadil, K.R.; Gewirth, A.A.; Shao, Y.; Gallagher, K.G. Sparingly solvating electrolytes for high energy density lithium-sulfur batteries. *ACS Energy Letters* **2016**, *1*, 503-509.
140. Lee, C.-W.; Pang, Q.; Ha, S.; Cheng, L.; Han, S.-D.; Zavadil, K.R.; Gallagher, K.G.; Nazar, L.F.; Balasubramanian, M. Directing the lithium-sulfur reaction pathway via sparingly solvating electrolytes for high energy density batteries. *ACS central science* **2017**, *3*, 605-613.



141. Shin, M.; Wu, H.-L.; Narayanan, B.; See, K.A.; Assary, R.S.; Zhu, L.; Haasch, R.T.; Zhang, S.; Zhang, Z.; Curtiss, L.A. Effect of the hydrofluoroether cosolvent structure in acetonitrile-based solvate electrolytes on the Li<sup>+</sup> solvation structure and li-s battery performance. *ACS applied materials & interfaces* **2017**, *9*, 39357-39370.
142. Bielejewski, M.; Puzkarska, A.; Tritt-Goc, J. Thermal properties, conductivity, and spin-lattice relaxation of gel electrolyte based on low molecular weight gelator and solution of high temperature ionic liquid. *Electrochimica Acta* **2015**, *165*, 122-129.
143. Kruk, D.; Wojciechowski, M.; Verma, Y.L.; Chaurasia, S.K.; Singh, R.K. Dynamical properties of EMIM-SCN confined in a SiO<sub>2</sub> matrix by means of <sup>1</sup>H NMR relaxometry. *Physical Chemistry Chemical Physics* **2017**, *19*, 32605-32616.
144. Ordikhani Seyedar, A.; Stapf, S.; Mattea, C. Nuclear magnetic relaxation and diffusion study of the ionic liquids 1-ethyl- and 1-butyl-3-methylimidazolium bis (trifluoromethylsulfonyl) imide confined in porous glass. *Magnetic Resonance in Chemistry* **2019**, *57*, 818-828.
145. Kowalczyk, J.; Bielejewski, M.; Tritt-Goc, J. Ionic liquid dynamics and electrical conductivity under confinement within micro and nanocellulose ionogels. *Cellulose* **2023**, 1-17.
146. Bielejewski, M.; Rachocki, A.; Kaszyńska, J.; Tritt-Goc, J. The gelation influence on diffusion and conductivity enhancement effect in renewable ionic gels based on a LMWG. *Physical Chemistry Chemical Physics* **2018**, *20*, 5803-5817.
147. Zavada, T.; Kimmich, R. The anomalous adsorbate dynamics at surfaces in porous media studied by nuclear magnetic resonance methods. The orientational structure factor and Lévy walks. *The Journal of chemical physics* **1998**, *109*, 6929-6939.
148. Kim, G.-T.; Appetecchi, G.B.; Alessandrini, F.; Passerini, S. Solvent-free, PYR1ATFSI ionic liquid-based ternary polymer electrolyte systems: I. Electrochemical characterization. *Journal of Power Sources* **2007**, *171*, 861-869.
149. Joost, M.; Kunze, M.; Jeong, S.; Schönhoff, M.; Winter, M.; Passerini, S. Ionic mobility in ternary polymer electrolytes for lithium-ion batteries. *Electrochimica Acta* **2012**, *86*, 330-338.
150. Li, M.; Yang, B.; Wang, L.; Zhang, Y.; Zhang, Z.; Fang, S.; Zhang, Z. New polymerized ionic liquid (PIL) gel electrolyte membranes based on tetraalkylammonium cations for lithium ion batteries. *Journal of membrane science* **2013**, *447*, 222-227.
151. Gouverneur, M.; Jeremias, S.; Schönhoff, M. <sup>7</sup>Li nuclear magnetic resonance studies of dynamics in a ternary gel polymer electrolyte based on polymeric ionic liquids. *Electrochimica Acta* **2015**, *175*, 35-41.
152. Shaplov, A.S.; Marcilla, R.; Mecerreyes, D. Recent advances in innovative polymer electrolytes based on poly (ionic liquid) s. *Electrochimica Acta* **2015**, *175*, 18-34.
153. Bhandary, R.; Schoenhoff, M. Polymer effect on lithium ion dynamics in gel polymer electrolytes: Cationic versus acrylate polymer. *Electrochimica Acta* **2015**, *174*, 753-761.
154. Shaplov, A.; Ponkratov, D.; Vygodskii, Y.S. Poly (ionic liquid) s: Synthesis, properties, and application. *Polymer Science Series B* **2016**, *58*, 73-142.
155. Wang, X.; Zhu, H.; Girard, G.M.; Yunis, R.; MacFarlane, D.R.; Mecerreyes, D.; Bhattacharyya, A.J.; Howlett, P.C.; Forsyth, M. Preparation and characterization of gel polymer electrolytes using poly (ionic liquids) and high lithium salt concentration ionic liquids. *Journal of Materials Chemistry A* **2017**, *5*, 23844-23852.
156. Kerner, M.; Johansson, P. Pyrrolidinium FSI and TFSI-based polymerized ionic liquids as electrolytes for high-temperature lithium-ion batteries. *Batteries* **2018**, *4*, 10.
157. Brinkkötter, M.; Gouverneur, M.; Sebastião, P.; Chávez, F.V.; Schönhoff, M. Spin relaxation studies of Li<sup>+</sup> ion dynamics in polymer gel electrolytes. *Physical Chemistry Chemical Physics* **2017**, *19*, 7390-7398.
158. Brinkkötter, M.; Lozinskaya, E.I.; Ponkratov, D.O.; Vygodskii, Y.; Schmidt, D.F.; Shaplov, A.S.; Schönhoff, M. Influence of cationic poly (ionic liquid) architecture on the ion dynamics in polymer gel electrolytes. *The Journal of Physical Chemistry C* **2019**, *123*, 13225-13235.
159. Tominaga, Y.; Yamazaki, K. Fast Li-ion conduction in poly (ethylene carbonate)-based electrolytes and composites filled with TiO<sub>2</sub> nanoparticles. *Chemical communications* **2014**, *50*, 4448-4450.
160. Lago, N.; Garcia-Calvo, O.; Lopez del Amo, J.M.; Rojo, T.; Armand, M. All-solid-state lithium-ion batteries with grafted ceramic nanoparticles dispersed in solid polymer electrolytes. *ChemSusChem* **2015**, *8*, 3039-3043.
161. Zhang, Z.; Zhang, Q.; Ren, C.; Luo, F.; Ma, Q.; Hu, Y.-S.; Zhou, Z.; Li, H.; Huang, X.; Chen, L. A ceramic/polymer composite solid electrolyte for sodium batteries. *Journal of Materials Chemistry A* **2016**, *4*, 15823-15828.
162. Xuefu, S.; Nemori, H.; Mitsuoka, S.; Xu, P.; Matsui, M.; Takeda, Y.; Yamamoto, O.; Imanishi, N. High Lithium-Ion-Conducting NASICON-Type Li<sup>+</sup> x Al x Ge y Ti<sub>2-x-y</sub> (PO<sub>4</sub>)<sub>3</sub> Solid Electrolyte. *Frontiers in Energy Research* **2016**, *4*, 12.

163. Yang, L.; Wang, Z.; Feng, Y.; Tan, R.; Zuo, Y.; Gao, R.; Zhao, Y.; Han, L.; Wang, Z.; Pan, F. Flexible composite solid electrolyte facilitating highly stable “soft contacting” Li–electrolyte interface for solid state lithium-ion batteries. *Advanced Energy Materials* **2017**, *7*, 1701437.
164. Peng, J.; Xiao, Y.; Clarkson, D.A.; Greenbaum, S.G.; Zawodzinski, T.A.; Chen, X.C. A Nuclear magnetic resonance study of cation and anion dynamics in polymer–ceramic composite solid electrolytes. *ACS Applied Polymer Materials* **2020**, *2*, 1180-1189.
165. Ding, C.; Nohira, T.; Kuroda, K.; Hagiwara, R.; Fukunaga, A.; Sakai, S.; Nitta, K.; Inazawa, S. NaFSA–ClC3pyrFSA ionic liquids for sodium secondary battery operating over a wide temperature range. *Journal of Power Sources* **2013**, *238*, 296-300.
166. Noor, S.A.M.; Howlett, P.C.; MacFarlane, D.R.; Forsyth, M. Properties of sodium-based ionic liquid electrolytes for sodium secondary battery applications. *Electrochimica Acta* **2013**, *114*, 766-771.
167. Monti, D.; Jónsson, E.; Palacín, M.R.; Johansson, P. Ionic liquid based electrolytes for sodium-ion batteries: Na<sup>+</sup> solvation and ionic conductivity. *Journal of Power Sources* **2014**, *245*, 630-636.
168. Ding, C.; Nohira, T.; Hagiwara, R.; Matsumoto, K.; Okamoto, Y.; Fukunaga, A.; Sakai, S.; Nitta, K.; Inazawa, S. Na [FSA]-[C3C1pyrr][FSA] ionic liquids as electrolytes for sodium secondary batteries: Effects of Na ion concentration and operation temperature. *Journal of Power Sources* **2014**, *269*, 124-128.
169. Pope, C.R.; Romanenko, K.; MacFarlane, D.R.; Forsyth, M.; O’Dell, L.A. Sodium ion dynamics in a sulfonate based ionomer system studied by <sup>23</sup>Na solid-state nuclear magnetic resonance and impedance spectroscopy. *Electrochimica Acta* **2015**, *175*, 62-67.
170. Guin, M.; Tietz, F. Survey of the transport properties of sodium superionic conductor materials for use in sodium batteries. *Journal of power sources* **2015**, *273*, 1056-1064.
171. Ma, Q.; Guin, M.; Naqash, S.; Tsai, C.-L.; Tietz, F.; Guillon, O. Scandium-substituted Na<sub>3</sub>Zr<sub>2</sub>(SiO<sub>4</sub>)<sub>2</sub>(PO<sub>4</sub>) prepared by a solution-assisted solid-state reaction method as sodium-ion conductors. *Chemistry of Materials* **2016**, *28*, 4821-4828.
172. Naqash, S.; Ma, Q.; Tietz, F.; Guillon, O. Na<sub>3</sub>Zr<sub>2</sub>(SiO<sub>4</sub>)<sub>2</sub>(PO<sub>4</sub>) prepared by a solution-assisted solid state reaction. *Solid State Ionics* **2017**, *302*, 83-91.
173. Zinkevich, T.; Fiedler, A.; Guin, M.; Tietz, F.; Guillon, O.; Ehrenberg, H.; Indris, S. Na<sup>+</sup> ion mobility in Na<sub>3</sub>+xSc<sub>2</sub>(SiO<sub>4</sub>)<sub>x</sub>(PO<sub>4</sub>)<sub>3-x</sub> (0.1 < x < 0.8) observed by <sup>23</sup>Na NMR spectroscopy. *Solid state ionics* **2020**, *348*, 115277.
174. Guin, M.; Tietz, F.; Guillon, O. New promising NASICON material as solid electrolyte for sodium-ion batteries: Correlation between composition, crystal structure and ionic conductivity of Na<sub>3</sub>+xSc<sub>2</sub>SixP<sub>3-x</sub>O<sub>12</sub>. *Solid State Ionics* **2016**, *293*, 18-26.
175. Gabriel, J.; Petrov, O.V.; Kim, Y.; Martin, S.W.; Vogel, M. Lithium ion dynamics in Li<sub>2</sub>S+ GeS<sub>2</sub>+ GeO<sub>2</sub> glasses studied using <sup>7</sup>Li NMR field-cycling relaxometry and line-shape analysis. *Solid state nuclear magnetic resonance* **2015**, *70*, 53-62.
176. Martin, S.W.; Bischoff, C.; Schuller, K. Composition Dependence of the Na<sup>+</sup> Ion Conductivity in 0.5 Na<sub>2</sub>S+ 0.5 [x GeS<sub>2</sub>+ (1-x) PS<sub>5</sub>/2] Mixed Glass Former Glasses: A Structural Interpretation of a Negative Mixed Glass Former Effect. *The Journal of Physical Chemistry B* **2015**, *119*, 15738-15751.
177. Storek, M.; Adjei-Acheamfour, M.; Christensen, R.; Martin, S.W.; Bohmer, R. Positive and negative mixed glass former effects in sodium borosilicate and borophosphate glasses studied by <sup>23</sup>Na NMR. *The Journal of Physical Chemistry B* **2016**, *120*, 4482-4495.
178. Watson, D.E.; Martin, S.W. Short range order characterization of the Na<sub>2</sub>S+ SiS<sub>2</sub> glass system using Raman, infrared and <sup>29</sup>Si magic angle spinning nuclear magnetic resonance spectroscopies. *Journal of Non-Crystalline Solids* **2017**, *471*, 39-50.
179. Shastri, A.; Watson, D.; Ding, Q.-P.; Furukawa, Y.; Martin, S.W. <sup>23</sup>Na nuclear magnetic resonance study of yNa<sub>2</sub>S+(1-y)[xSiS<sub>2</sub>+(1-x)PS<sub>5</sub>/2] glassy solid electrolytes. *Solid State Ionics* **2019**, *340*, 115013.
180. Anderson, O.; Stuart, D. Calculation of activation energy of ionic conductivity in silica glasses by classical methods. *Journal of the American Ceramic Society* **1954**, *37*, 573-580.
181. Haaks, M.; Martin, S.W.; Vogel, M. Relation of short-range and long-range lithium ion dynamics in glass-ceramics: Insights from Li <sup>7</sup> NMR field-cycling and field-gradient studies. *Physical Review B* **2017**, *96*, 104301.
182. Becher, M.; Becker, S.; Hecht, L.; Vogel, M. From local to diffusive dynamics in polymer electrolytes: NMR studies on coupling of polymer and ion dynamics across length and time scales. *Macromolecules* **2019**, *52*, 9128-9139.
183. Sinai, Y.G. The limiting behavior of a one-dimensional random walk in a random medium. *Theory of Probability & Its Applications* **1983**, *27*, 256-268.
184. Oshanin, G.; Burlatsky, S.; Moreau, M.; Gaveau, B. Behavior of transport characteristics in several one-dimensional disordered systems. *Chemical physics* **1993**, *177*, 803-819.
185. Kariyo, S.; Brodin, A.; Gainaru, C.; Herrmann, A.; Hintermeyer, J.; Schick, H.; Novikov, V.; Rössler, E. From simple liquid to polymer melt. Glassy and polymer dynamics studied by fast field cycling NMR relaxometry: Rouse regime. *Macromolecules* **2008**, *41*, 5322-5332.

**Disclaimer/Publisher's Note:** The statements, opinions and data contained in all publications are solely those of the individual author(s) and contributor(s) and not of MDPI and/or the editor(s). MDPI and/or the editor(s) disclaim responsibility for any injury to people or property resulting from any ideas, methods, instructions or products referred to in the content.